Dynamic Calibration of Pressure Sensors

Mikael Nilsson

LUND UNIVERSITY

Department of Automatic Control

MSc Thesis
TFRT-6008-SE
ISSN 0280-5316

Department of Automatic Control
Lund University
Box 118
SE-221 00 LUND
Sweden

Printed in Sweden by Tryckeriet i E-huset
Lund 2016

Abstract

English

This master thesis is a project report of a system identification experiment of pressure sensors in order to characterise their frequency behaviour. The information about the frequency behaviour is for example very useful in the automotive industry, where pressure sensors are used to measure the dynamic pressures in combustion engines. The sensors are identified by means of impulse response analysis using the Ho and Kalman algorithm based on the use of Markov parameters. The sensors presented in the thesis were identified with a certain level of success, and conclusions such as resonant frequencies and bandwidth could be drawn.

This master thesis project is performed in collaboration with SP Technical Research Institute of Sweden.

Svenska

Den här rapporten redogör för systemidentifiering av trycksensorer, och genom modellering och experiment karakteriseras sensorernas frekvensbeteende. Information om trycksensorers frekvensbeteende är särskilt användbart i bilindustrin där trycksensorer används för att mäta dynamiska tryckförlopp i förbränningsmotorer. Trycksensorerna identifieras med hjälp av impulssvarsanalys via en algoritm från Ho och Kalman som använder sig av Markov-parametrar. Sensorerna som presenteras i den här rapporten identifierades med viss framgång, och egenskaper såsom resonanser och bandbredd kunde bestämmas.

Det här examensarbetet har genomförts i samarbete med SP Sveriges Tekniska Forskningsinstitut.

Acknowledgements

The author would like to take the opportunity to express his gratitude to his supervisors in this project, Dr. Rolf Johansson at Lund University and Dr. Martin Zelan at SP Technical Research Institute of Sweden. They have both been very helpful in offering guidance and support during this master thesis project.

Contents

1

Introduction

This report will account for the purpose, methods and results of the master thesis project *Dynamic calibration of pressure sensors*. This first chapter will give a short introduction to the layout of the thesis, as well as stating the purpose of this thesis. The second chapter outlines the historical background to dynamic calibration, and the third and fourth chapters will in detail entail the method and the results. Finally, the fifth and sixth chapters will discuss the results and present a conclusion and some advise for further studies and experimentation.

The need of well defined standardised units is usually obvious to a scientist or engineer. Without standardised units and calibrated measurement equipment it would be hard to collaborate and for example send a rocket into space. The scientific field of static calibration is well developed and continually seeks out new and better definitions of the standardised units, in order to achieve more reliable calibrations. Dynamic calibration on the other hand considers the sensor's frequency behaviour, and invites the engineer to distrust the readings of the measuring device when measuring a dynamic signal. The statically calibrated measuring device does not necessarily give a true account of a dynamic signal, as it might resonate, dampen or delay the measured dynamic quantity. This thesis project partakes in the research towards a standardised method within the field of dynamic calibration.

2

Background

This chapter will outline the background history behind this thesis project, and it will start with a short account of SP Technical Research Institute of Sweden, the institute where this thesis project was performed at.

2.1 SP Technical Research Intitute of Sweden

SP Technical Research Institute of Sweden [www.sp.se], abbreviated SP, is a governmentally owned research institute with a national directive to perform research and offer services, which are essential but not always financially sustainable for the Swedish industry. SP is also designated as the national metrology institute, which means that they have a responsibility to facilitate and maintain Sweden's standard SI units and their basis definitions: the kilo, the metre and the second being among them.

One of the departments connected to the designation national metrology institute is the department of Measurement Technology. A subdivision of Measurement Technology is the division *Pressure and Vacuum*, where they among many services perform calibration of pressure sensors. This thesis was performed at this subdivision.

2.2 Calibration of pressure sensors

Calibration is typically made under static conditions. In the case of calibrating pressure sensors, the sensor to be calibrated (also called Device Under Test, abbreviated DUT) is mounted in an apparatus, where it is exposed to a defined pressure with established error bounds, traceable to the definition of pressure. The process is then repeated for various different defined static pressures. A proof document is then formulated containing the measured values of the DUT together with the error bounds of each measurement. The calibration document also contains a reference of how the measurements where produced, and how it traces back to the definition of pressure.

This procedure of calibrating pressure sensors is highly valuable in order to facilitate accurate measurements of static pressure. However, statically calibrated sensors are also used to measure pressure in environments where the pressure is changing at various rates, for example, in a combustion engine. If the statically calibrated sensor starts to dampen the signal or resonate at certain frequencies, then it would inherently give a false measurement reading.

At the moment there does not exist an internationally agreed standard for dynamic calibration of pressure sensors, but there are however several documented approaches or methods for performing a dynamic calibration [Hjelmgren, 2002]. One dominating approach, inspired by the field of system identification, is to expose the sensor to an impulse pressure signal and then analyse its frequency characteristics. Since dynamic calibration is not standardized there does not exist an agreement on relevant aspects of the analysis in the calibration. However, bandwidth, rise time and resonant frequencies of the sensor are typically interesting conclusions of the analysis [Hjelmgren, 2002].

A popular non-standardised implementation of an impulse pressure signal is *the shock tube*. A shock tube consists of two elongated chambers, with a constant cross area, separated by a burst diaphragm. Initially the gas pressure is higher in one chamber than in the other. When the diaphragm ruptures the expansion of the high-pressure gas into the low-pressure chamber generates a shock wave which travels faster than the expanding gas. The rise time of the pressure is in the order of nanoseconds and it is considered to be an ideal pressure impulse.

Dynamic calibration of pressure sensors is on demand from the Swedish industry, and SP is currently investing resources researching the subject. SP has chosen the shock tube method, as it is fairly simple to implement and it is showing great promise of becoming a standard method for dynamic calibration.

3

Method

This chapter will outline the method by which the frequency characteristics of a pressure sensor is identified. The Sections 3.1 to 3.4 concern the experiment setup, the sensor types to be characterized and the execution of an experiment, and the Sections 3.5 to 3.6 concern shock wave theory and sensor modelling. Finally the last section, Section 3.7, concerns the Ho and Kalman algorithm used to estimate a state-space representation of impulse response data.

3.1 The shock tube

The shock tube consists of two elongated cylindrical chambers, with a constant cross section, separated by a burst diaphragm. At the start of an experiment, the gas pressure is higher in one chamber than in the other. The chamber with higher initial pressure is labelled *Driver* and the chamber with lower initial pressure is labelled *Driven*.

A pressure sensor to be characterised, denoted Device Under Test or *DUT* in short, is mounted in the end flange of the Driven chamber. Two secondary pressure sensors are mounted on the side of the Driven and Driver chamber, respectively. The sensor on the Driven chamber, together with the DUT and the known distance between them, are used to estimate the velocity of the shock wave. The exact burst pressure of the diaphragm is unknown, which is why a secondary pressure sensor is mounted on the side of the Driver chamber in order to know the static pressure at the time of the diaphragm burst.

A simplified illustration of the shock tube is shown in Figure 3.1, and a more detailed overview of the shock tube and its dimensions can be found in Appendix A.

Three vents are connected to the Driver end flange. Two are connected to a pressure source, with a nominal pressure of 7.5 Bar. The third vent is unconnected and is used to de-pressurize the tube to atmospheric pressure. The vents are manually operated from an electrical cabinet. A more detailed schematic of the experiment set-up and its connections can be found in Appendix B.

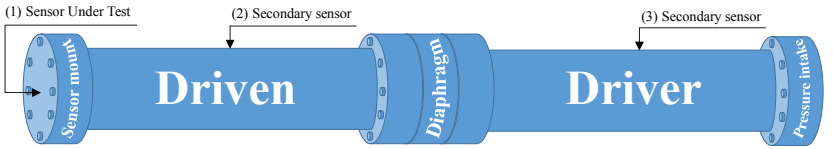

Figure 3.1 The shock tube with indicated sensor positions. The burst-diaphragm is mounted in the cross-section inbetween the *Driver* and *Driven* tube-sections. The pressure intake is mounted at the starting end of the Driver-section. (1) Mounting-position for sensor to be tested. (2) Mounting-position for velocity detecting sensor. (3) Mounting-position for static pressure sensor.

3.2 Data acquisition

The signal data from the pressure sensors are sampled using a data acquisition system from *National Instruments*, capable of sampling rates up to 100 MHz. The data acquisition hardware is listed in Table 3.1.
The signal data is acquired and saved to file using the software *NI Signal Express* from National Instruments.

Table 3.1 List of data acquisition hardware

Name	Description
NI PXIe 1062Q	Data acquisition computer
NI PXIe 8106	Computer interface for communication with automated equipment
NI PXI 4462	2 units with 24-bit resolution, 4-Input dynamic signal analyzer, sampling rates up to 200 kHz
NI PXIe 5122	Sampling rates up to 100 MHz, 14-Bit Oscilloscope/Digitizer

3.3 Pressure sensors

In this thesis two types of pressure sensors are tested: a piezoelectric pressure sensor and fiber-optic pressure sensors. The raw signal outputs from each of the sensor categories are all relatively small, so all sensors to be tested will be routed through a suitable signal conditioner and amplifier. The exact sensor and manufacturer of each sensor type can not be disclosed in this thesis, instead a brief description of the sensors are given.

Piezoelectric pressure sensors

A piezoelectric sensor uses the piezoelectric effect in order to measure changes in pressure by converting the applied pressure to an electrical charge. The registered output is linearly proportional to the derivative pressure change. In order to measure static pressure the signal will have to be converted and amplified.

Fiber-optic pressure sensors

A fiber-optic sensor works by guiding a LED light source through an optical fiber ending in a Fabry–Perot like cavity. The Fabry–Perot cavity of the sensors in this thesis consists of an etched hole in a silicon membrane bounded to a Pyrex-glass. When pressure is applied to the cavity it deforms the membrane and changes the cavity length, hence changing the amount of reflected light [Zelan et al., 2015] [Hjelmgren, 2002]. The intensity of the reflected light is then detected by a photodiode, and the relation between pressure and light intensity is approximately linear in a certain pressure interval. Figure 3.3 illustrates the mentioned cavity, and Figure 3.2 shows an approximate calculation of the reflectivity as a function of cavity length. The thick black line in the curve marks the typical working region of the sensor.

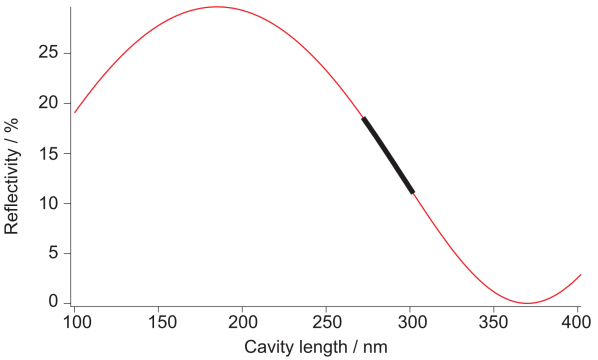

Figure 3.2 Illustration of reflected light intensity versus Cavity length. The black line indicates the working region of the sensor [Zelan et al., 2015].

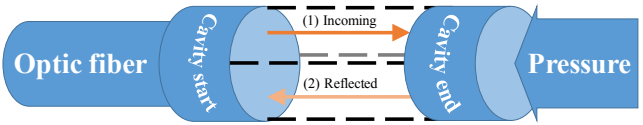

Figure 3.3 The Fabry-Perot cavity of the optical pressure sensor. The figure illustrates how the incoming light is reflected with an intensity relative to the applied pressure on the cavity end.

3.4 Experiment procedure

The diaphragm consists of thin circular cellophane sheets. Different shock wave pressure amplitudes are generated by varying the number of sheets in the removable middle section of the shock tube. An experiment execution starts by unbolting the diaphragm holder from between the Driver and Driven tubes, and vacuum cellophane residue from the tubes and then mount a new set of cellophane sheets in the holder. The diaphragm holder is afterwards mounted back in place. The Driver tube is pressurised by manually activating the vents to the pressure source, and at the same time the data acquisition software is manually initiated. The vents are manually closed at the sound of diaphragm burst, and a few seconds later the acquisition software is finished gathering a set of sampled data from the sensors. The shock tube is then de-pressurized by manually activating a third vent.

The shock tube is made of steel and is grounded to earth in order to minimize any potential electrical interference in the electrical sensors. All the electrical support equipment are also grounded to the same earth potential.

3.5 Shock wave theory

When the diaphragm bursts, the expansion of the high-pressure Driver gas into the low-pressure Driven gas generates a shock wave travelling faster than the expanding gas. The shock wave has a width or thickness of a few hundred nanometres so as to an observer at rest, the pressure across a shock wave moving at about 500 m/s rises from the Driven chamber's initial pressure to a relatively constant post-shock pressure in a time period of the order of a nanosecond [Zelan et al., 2015]. The pressure remains constant for a few milliseconds as the shock wave is being reflected in the Driven flange. The impulse of the shock wave at the Driven flange depends on the dimensions of the tube, sensor location in the Driven flange, the type of gas used in the Driver and Driven chambers, as well as the initial pressures and temperatures measured just before the moment when the diaphragm bursts.

The measured change in pressure as the shock wave hits the DUT can be considered to be an impulse response. The resulting pressures, temperatures and densities

generated within the shock tube as the shock wave propagates can be derived from ideal gas theory [Teichter, 2005] [Oakley, 2016] [Anderson, 2002]. Figure 3.4 illustrates time snapshots of the propagation of the shock wave from the moment the diaphragm burst until it is reflected in the end flange of the Driven tube.

The indicated pressure variables point out the volumes of pressure that can be theoretically estimated using Equations 3.1 to 3.10 [Anderson, 2002].

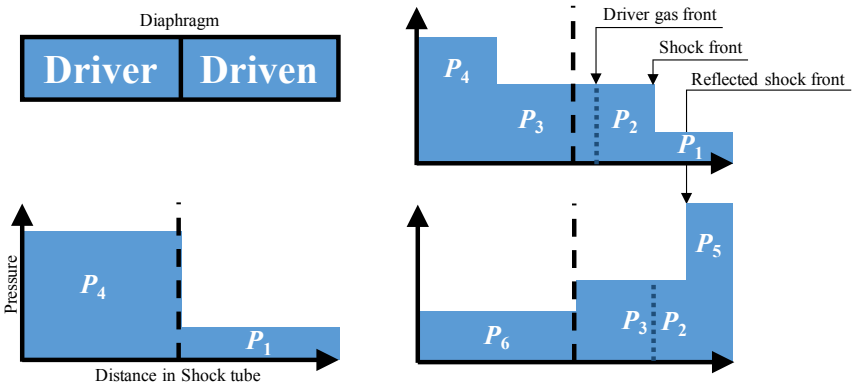

Figure 3.4 Illustration of shockwave propagation. The illustration is interpreted from top to bottom, left to right. P_1 and P_4 are the initial pressures. $P_2 = P_3$ are the pressures generated behind the shock-wave. P_5 is the reflected pressure, and is also the detected shock-wave pressure. P_6 is the trailing pressure as the shock-wave is being reflected.

Table 3.2 List of equation variables for Equations 3.1 to 3.10.

Variable	Description
a	velocity of sound [m/s]
W	velocity of shock wave [m/s]
u_2	particle velocity [m/s]
M	Mach number $= \frac{W}{a}$
p	pressure [Pa]
T	temperature [K]
γ	specific heat ratio
ρ	density [kg/m^3]

$$\frac{p_2}{p_1} = 1 + \frac{2\gamma}{\gamma+1}\left(M^2 - 1\right) \tag{3.1}$$

$$\frac{T_2}{T_1} = \frac{p_2}{p_1}\left(\frac{\frac{\gamma+1}{\gamma-1} + \frac{p_2}{p_1}}{1 + \frac{\gamma+1}{\gamma-1}\left[\frac{p_2}{p_1}\right]}\right) \tag{3.2}$$

$$\frac{\rho_2}{\rho_1} = \frac{1 + \frac{\gamma+1}{\gamma-1}\left(\frac{p_2}{p_1}\right)}{\frac{\gamma+1}{\gamma-1} + \frac{p_2}{p_1}} \tag{3.3}$$

$$u_2 = \frac{a_1}{\gamma}\left(\frac{p_2}{p_1} - 1\right)\left(\frac{\frac{2\gamma}{\gamma+1}}{\frac{p_2}{p_1} + \frac{\gamma-1}{\gamma+1}}\right)^{1/2} \tag{3.4}$$

$$\frac{p_5}{p_2} = \frac{(3\gamma-1)\frac{p_2}{p_1} - (\gamma-1)}{(\gamma-1)\frac{p_2}{p_1} + (\gamma+1)} \tag{3.5}$$

$$\frac{T_5}{T_2} = \frac{p_5}{p_2}\left(\frac{\frac{\gamma+1}{\gamma-1} + \frac{p_5}{p_2}}{1 + \frac{\gamma+1}{\gamma-1}\left[\frac{p_5}{p_2}\right]}\right) \tag{3.6}$$

$$\frac{\rho_5}{\rho_2} = \frac{1 + \frac{\gamma+1}{\gamma-1}\left(\frac{p_5}{p_2}\right)}{\frac{\gamma+1}{\gamma-1} + \frac{p_5}{p_2}} \tag{3.7}$$

$$W_R = (\rho_2 u_2)/(\rho_5 - \rho_2) \tag{3.8}$$

$$M_R = (W_R + u_2)/(a_2) \tag{3.9}$$

$$\frac{p_4}{p_1} = \frac{p_2}{p_1}\left(1 - \frac{(\gamma_4 - 1)(a_1/a_4)(p_2/p_1 - 1)}{\sqrt{2\gamma_1\left[2\gamma_1 + (\gamma_1+1)(p_2/p_1 - 1)\right]}}\right)^{-2\gamma_4/(\gamma_4-1)} \tag{3.10}$$

3.6 Sensor model

The pressure sensors can be modelled by a second order linear, time-invariant physical model with a mass m, stiffness k and viscous damping c, illustrated in Figure 3.5.

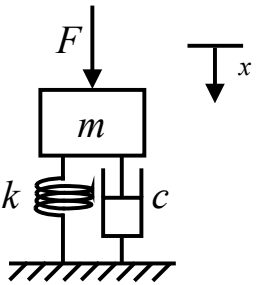

Figure 3.5 A linear time-invariant model of a pressure sensor.

The differential equation of this model is shown in Equation 3.11.

$$m\ddot{x}(t) + c\dot{x}(t) + kx(t) = F(t) \tag{3.11}$$

Equation 3.11 can be rewritten on the form in Equation 3.12, where ω_n is the undamped natural frequency and ζ is the relative damping [Hjelmgren, 2002].

$$\begin{aligned} \ddot{x}(t) + 2\zeta\omega_n\dot{x}(t) + \omega_n^2 x(t) &= \frac{F(t)}{m} \\ \omega_n = \sqrt{\frac{k}{m}}, \qquad \zeta &= \frac{c}{2m\omega_n} \end{aligned} \tag{3.12}$$

The solution to Equation 3.12, with initial conditions according to 3.13, is shown in Equation 3.14.

$$x(0) = x_0, \quad \dot{x}(0) = 0, \quad F(t) = 0 \tag{3.13}$$

$$\begin{aligned} x(t) = x_0 e^{-\zeta\omega_n t} &\left(\frac{\zeta}{\sqrt{1-\zeta^2}} \sin(\omega_d t) + \cos(\omega_d t) \right) \\ &+ \frac{1}{m\omega_d} \int_0^t F(t-\tau) e^{-\zeta\omega_n \tau} \sin(\omega_d \tau) d\tau \\ \omega_d = \sqrt{1-\zeta^2}\omega_n & \end{aligned} \tag{3.14}$$

When the force F is a sinusoidal function the sensor response is given by

$$x(t) = |G(\omega)|F\sin(\omega t - \phi) \tag{3.15}$$

with the transfer function $G(\omega)$ given by

$$G(\omega) = \frac{\frac{1}{k}}{1 - \left(\frac{\omega}{\omega_n}\right)^2 + i2\zeta\left(\frac{\omega}{\omega_n}\right)} \tag{3.16}$$

and the amplitude response $|G(\omega)|$ and phase shift ϕ are given by

$$\begin{aligned} |G(\omega)| &= \frac{\frac{1}{k}}{\sqrt{\left(1 - \left(\frac{\omega}{\omega_n}\right)^2\right)^2 + 4\zeta^2\left(\frac{\omega}{\omega_n}\right)^2}} \\ \phi &= \arctan\left(\frac{2\zeta\frac{\omega}{\omega_n}}{1 - \left(\frac{\omega}{\omega_n}\right)^2}\right) \end{aligned} \tag{3.17}$$

3.7 Data processing

The data is processed in Matlab according to the following schedule.

1. Visual inspection of the raw data.
2. Isolate the samples around the impulse response from the shock wave, and remap the step between zero and one. Zero being the level before the response and one being the settling value.
3. Perform frequency spectrum analysis on the remapped data and search for resonant frequencies.
4. Perform Principal Component Analysis in an effort to separate signal from noise.
    a) Display how much of the data is being represented by the principal components.
    b) Analyse residuals for frequency content.
    c) Merge the reconstructed signals from the principal component analysis to get one representative signal for the impulse response analysis.
    d) Re-sample the data to a meaningful lower frequency with respect to the detected resonant frequency.
5. Programmatically detect the start of the response, and send the resulting samples to the Ho-Kalman algorithm for impulse response analysis.

The Ho-Kalman algorithm is based on the use of Markov parameters, and is designed to estimate a state-space model from impulse response data [Johansson, 2012]. You start by arranging the impulse response parameters in a Hankel matrix of the form in Equation 3.18.

$$
\begin{aligned}
H_{rs}^{(k)} &= \begin{bmatrix} H_{k+1} & H_{k+2} & \dots & H_{k+s} \\ H_{k+2} & H_{k+3} & \dots & H_{k+s+1} \\ \vdots & \vdots & \ddots & \vdots \\ H_{k+r} & H_{k+r+1} & \dots & H_{k+r+s-1} \end{bmatrix} \\
&= \begin{bmatrix} CA^kB & CA^{k+1}B & \dots & CA^{k+s-1}B \\ CA^{k+1}B & CA^{k+2}B & \dots & CA^{k+s}B \\ \vdots & \vdots & \ddots & \vdots \\ CA^{k+r-1}B & CA^{k+r}B & \dots & CA^{k+r+s-1}B \end{bmatrix}
\end{aligned}
\tag{3.18}
$$

$$
k = 0, 1, 2, 3, \dots \text{ (sample index), and } \quad r, s = \left\lfloor \frac{\text{length(samples)}}{2} \right\rfloor - 1
$$

Using Matlab you then compute the singular value decomposition of $H_{rs}^{(0)}$ as shown in Equation 3.19, and by plotting the eigenvalues in a lin-log plot you get information about the model order of your desired state-space realisation. After selecting a desired model order, the relationship between the Hankel matrix, the singular value decomposition and the A, B, C and D matrices of the state-space realization is shown in Equations 3.19 to 3.24.

$$H_{rs}^{(0)} = U\Sigma V^T \tag{3.19}$$

$$\begin{aligned} \Sigma_n &= \text{diag}\{\sigma_1, \sigma_2, ..., \sigma_n\} \\ U_n &= \text{matrix of first } n \text{ columns of U} \\ V_n &= \text{matrix of first } n \text{ columns of V} \\ n &= \text{chosen model order} \end{aligned} \tag{3.20}$$

$$\begin{aligned} E_y = \begin{bmatrix} I_{p\times p} & 0_{p\times(r-1)p} \end{bmatrix}^T, \quad E_u = \begin{bmatrix} I_{m\times m} & 0_{m\times(s-1)m} \end{bmatrix}^T \\ p = \text{number of outputs}, \quad m = \text{number of inputs} \end{aligned} \tag{3.21}$$

$$\begin{aligned} A_n &= \Sigma_n^{-1/2} U_n^T H_{rs}^{(1)} V_n \Sigma_n^{-1/2} \\ B_n &= \Sigma_n^{1/2} V_n^T E_u \\ C_n &= E_y^T U_n \Sigma_n^{1/2} \\ D &= H_0 \end{aligned} \tag{3.22}$$

$$\begin{aligned} x_{k+1} &= A_n x_k + B_n u_k \\ y_k &= C_n x_k + D u_k \end{aligned} \tag{3.23}$$

$$H(z) = C_n(zI - A_n)^{-1} B_n + D \tag{3.24}$$

A Matlab implementation of the Ho-Kalman algorithm can be found in Appendix D.

4

Results

This section of the report accounts for the results of the experiments.

4.1 Acquired signals and shock wave theory

An exact burst pressure can not be established due to the use of non-identical cellophane sheets, so therefore three ranges of pressure characteristics are established: *Low* pressure, *Medium* pressure and *High* pressure. This simply translates into 2, 4 or 6 sheets of cellophane used as a diaphragm. Three sets of signals are acquired in each experiment. Figure 4.1 shows from left to right the electrical signals acquired and converted to pressure from a Low, Medium and High pressure experiment:

1. Driven end flange, *the DUT*.
2. Driven side, *used together with the data from the DUT to estimate shock wave velocity*.
3. Driver side, *measuring the static pressure*.

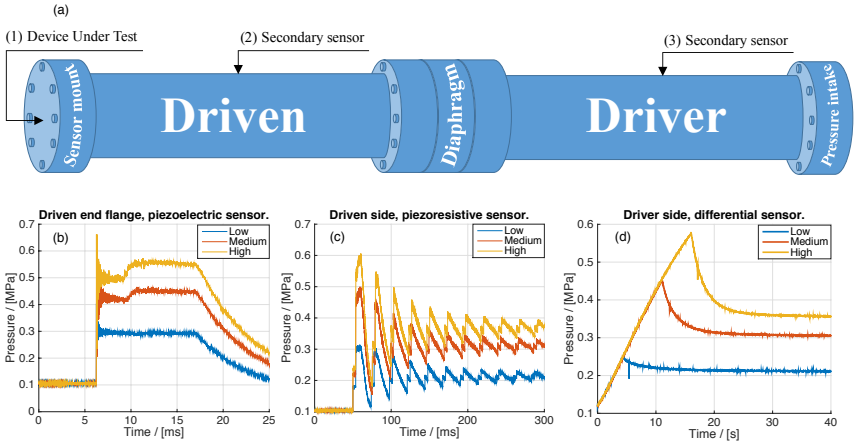

Figure 4.1 Acquired signals. (a) illustrates the shock-tube. (b) sampled data from position 1 - device under test. (c) sampled data from 2 - secondary sensor, used together with the DUT signal to estimate shock wave velocity. (d) sampled data from 3 - secondary sensor, slow stationary pressure.

To theoretically confirm the system, a comparison between measured data from a High pressure experiment, see Figure 4.2, and theoretical calculations using the equations from Chapter 3.5 are shown in Table 4.2. The data from Figure 4.2 is then compared to the theoretical data in Table 4.2. The starting values for the calculations are temperature and pressure in the Driven section, and the temperature of the Driver section at the moment the diaphragm bursts, as well as the shock wave velocity estimated from the sampled data, see Table 4.1.

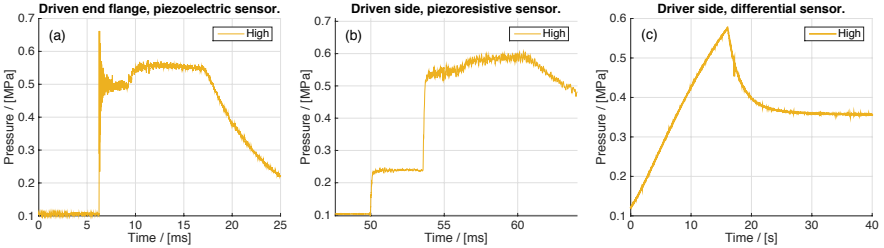

Figure 4.2 Sampled data from a *High*-pressure experiment. (a) sampled data from position 1 - device under test. (b) sampled data from 2 - secondary sensor. (c) sampled data from 3 - secondary sensor.

Table 4.1 Input variables to the data in Table 4.2.

Description	**Value**
Shock wave velocity	512.8 m/s
Shock wave Mach number	$\frac{512.8}{344.1}$ m/s = 1.49
Burst pressure Driven	0.1011 MPa
Burst temperature Driver	295.35 K
Burst temperature Driven	294.15 K
Molar mass Air	28.966
Specific heat ratio Air	1.402

Table 4.2 Theoretical calculations, based on Equations 3.1 to 3.10.

Type	[P_1] **Driven**	[P_2] **Shocked**	[P_4] **Driver**	[P_5] **Reflected**	**Unit**
Pressure	0.101	0.245	0.685	0.536	*MPa*
Temp	294.2	386.9	295.4	490.7	*K*
Density	1.197	2.209	8.078	3.803	kg/m^3
Sound vel.	344.1	394.6	344.8	444.4	*m/s*
Particle vel.	0	234.8	0	0	*m/s*
Approximated initial driver pressure			0.584 MPa		

The pressure values from Table 4.2 belonging to the columns *Driven*, *Shocked* and *Reflected* are quite close to the measured values in the second figure of Figure 4.2. Where the measured values in Figure (4.2 b) upto 50 ms is compared to *Driven*, the value between ~50-54 ms is compared to *Shocked* and the value between ~54-56 ms is compared to *Reflected*. In Figure (4.2 a), the first step-like settling value is compared to *Reflected*. The Driver burst pressure is also estimated and shown in Table 4.1 and is compared to the peak value of Figure (4.2 c). The shock wave velocity was estimated from dually sampled data from the DUT and the Driven secondary sensor by programmatically detecting the signal rise from the two signals. By taking the calculated time in-between together with the known distance between them an estimation of the shock wave velocity could be calculated.

Figure 4.3 illustrates the shock wave front as well as the Driver gas front in measured data from a Device Under Test, which could be determined from the calculated particle velocity and estimated shock wave velocity from Table 4.2 and Table 4.1 respectively.

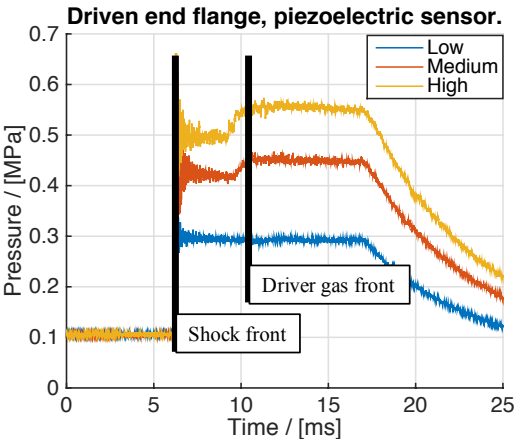

Figure 4.3 The front of the shock wave and the driver gas identified by velocity estimation.

4.2 Goodness of fit

In the Sections 4.3 to 4.7 the data processing and impulse response analysis will be presented for the five different sensors. The identified state-space systems for the sensor will be subject to impulse simulations and a goodness of fit is calculated and shown together with the simulations. The goodness of fit is calculated by means of of the Root Mean Square error criterion:

$$FIT\% = 1 - \frac{\left\| \overline{\text{signal}} - \overline{\text{signal generated from model}} \right\|_2}{\left\| \overline{\text{signal}} - mean(\overline{\text{signal}}) \right\|_2} \tag{4.1}$$

The same method is used in the System Identification Toolbox in Matlab, and a high percentage score indicates a good model fit to the original data.

4.3 Piezoelectric sensor

Figure 4.4 shows the raw data sampled at 100MHz from the piezoelectric sensor.

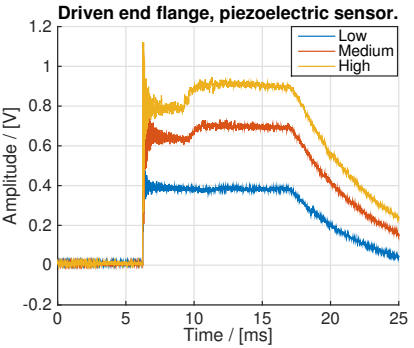

Figure 4.4 Raw data from the piesoelectric sensor, sampled at 100MHz.

Data processing and impulse response analysis

Figure 4.5 illustrates the remapped data, and Figure 4.6 shows the power spectrum of the remapped data with a label indicating an identified resonant frequency at 318 kHz. Table 4.3 shows the amount of data represented by each principal component. The first principal component has an accounting percentage of 99.6%, which is considered sufficient enough. Figure 4.7 and Figure 4.8 show the reconstructed signals from the first principal component and the residuals of each reconstruction respectively. Figures 4.9 to 4.11 show the residual autocovariance of each residual, and they all indicate that the residuals are not purely white for low frequencies. Figure 4.12 shows the power spectrum of the residuals and it illustrates that the residuals still contain information about the resonant frequency, but also a low frequency at around 6.8 kHz.

The reconstructed signals from the first principal component are then averaged point by point in order to get one representative signal for impulse response analysis, see Figure 4.13. This is motivated by visual inspection of the reconstructed data which showed the signals to be exactly the same, only with an amplitude difference. The averaged signal is then resampled to a lower frequency with respect to the identified resonant frequency, in this case 1MHz, and the step-like start is then detected programmatically and sent to the Ho-Kalman algorithm, see Figure 4.14.

The singular values retrieved from the singular value decomposition of $H_{rs}^{(0)}$ are shown in Figure 4.15, and indicates the appropriate choice of model order. Figure 4.16 shows the result of an impulse simulation with a model of order 100. The high order is motivated by the effort to model the high frequency behaviour of the

original data. Figures 4.18 and 4.20 illustrate the z-transform pole-zero plane and Bode diagram of the state-space system of order 100 respectively.

Figure 4.15 shows that the piezoelectric sensor could be modelled as simply as a system of order 2, which corresponds quite well with the sensor model described in Section 3.6. Figure 4.17 shows the result of an impulse simulation with a model of order 2. Figures 4.19 and 4.21 illustrate the z-transform pole-zero plane and Bode-diagram of the state-space system of order 2 respectively.

The 100th order model got a goodness of fit score of 8.28%, and the second order model got a score of 7.16%. Visually the two models seems to fit the original data well, in regards to settling value and signal curvature. The low score could be explained by the original data having a low signal to noise ratio.

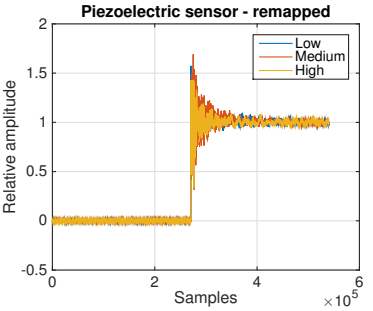

Figure 4.5 Remapped data.

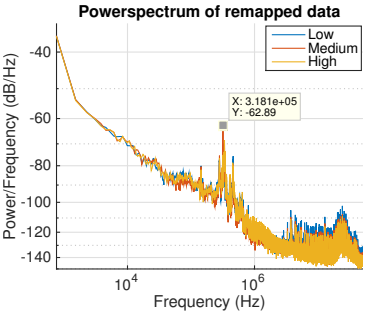

Figure 4.6 Remapped data, spectrum.

Table 4.3 Principal components, piezoelectric sensor.

Principal component	Accounts for
1 PC	99.6196%
2 PC	99.8938%
3 PC	100%

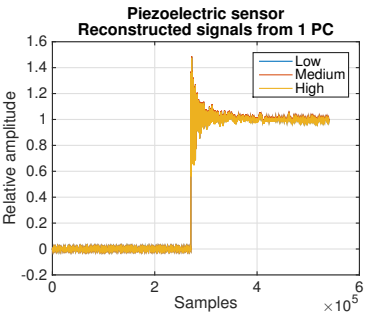

Figure 4.7 1 PC.

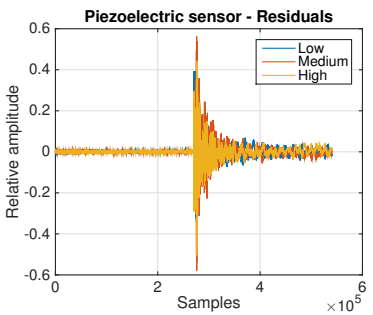

Figure 4.8 1 PC - residuals.

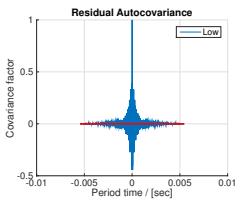

Figure 4.9 Low - resid. autocovariance.

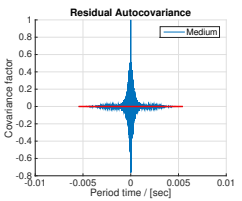

Figure 4.10 Medium - resid. autocovariance.

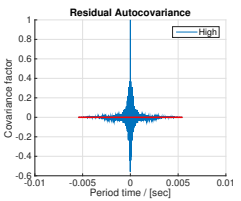

Figure 4.11 High - resid. autocovariance.

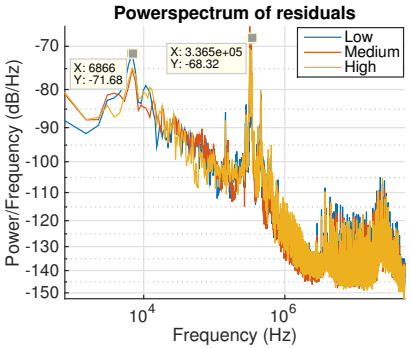

Figure 4.12 Residuals - power spectrum.

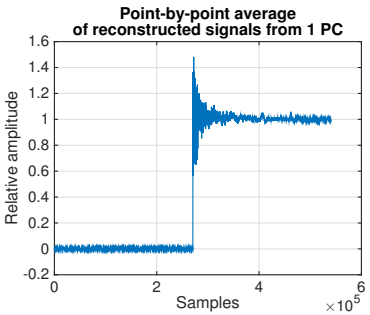

Figure 4.13 1 PC - averaged.

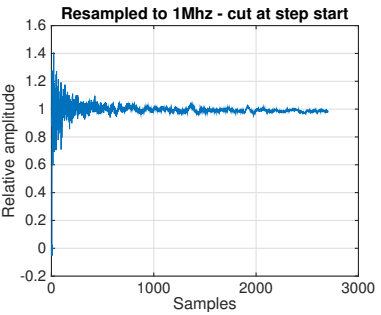

Figure 4.14 Input to Ho-Kalman.

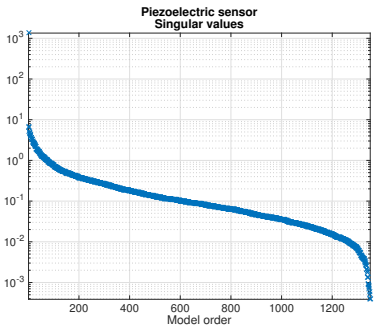

Figure 4.15 Singular values.

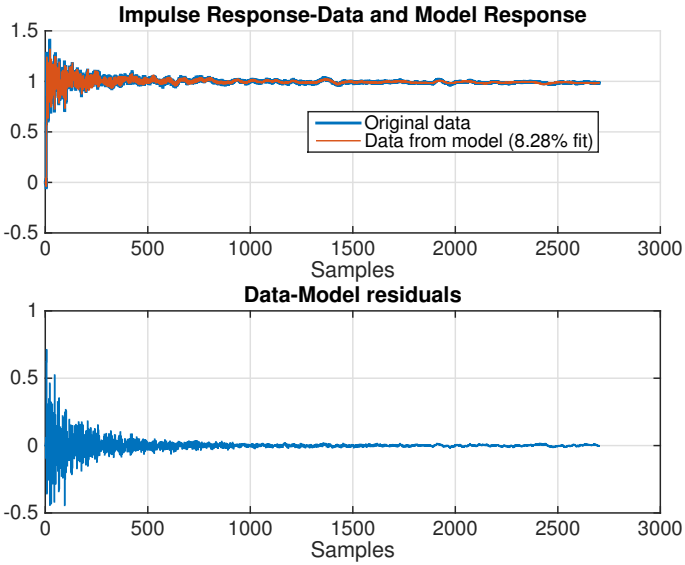

Figure 4.16 Impulse simulation 100th order.

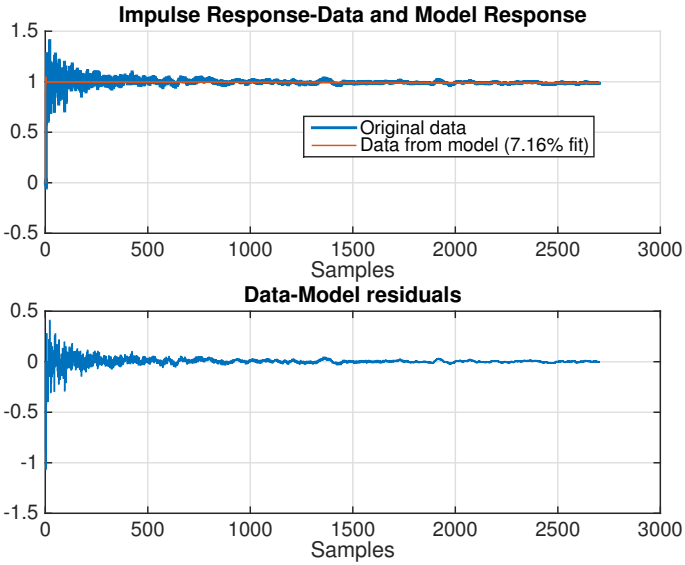

Figure 4.17 Impulse simulation 2nd order.

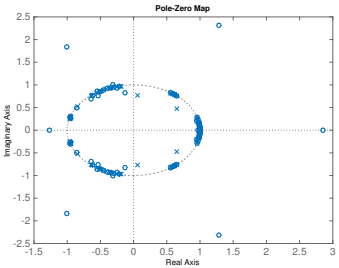

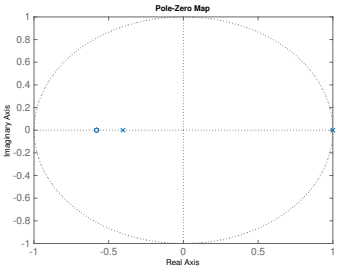

Figure 4.18 Pole-zero map 100th order. **Figure 4.19** Pole-zero map 2nd order.

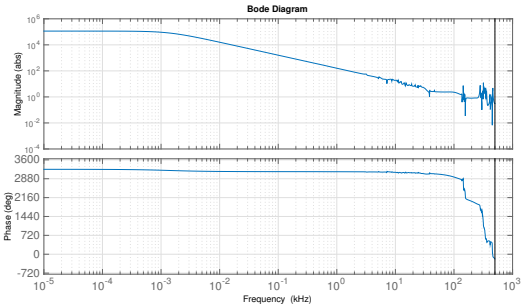

Figure 4.20 Bode diagram 100th order.

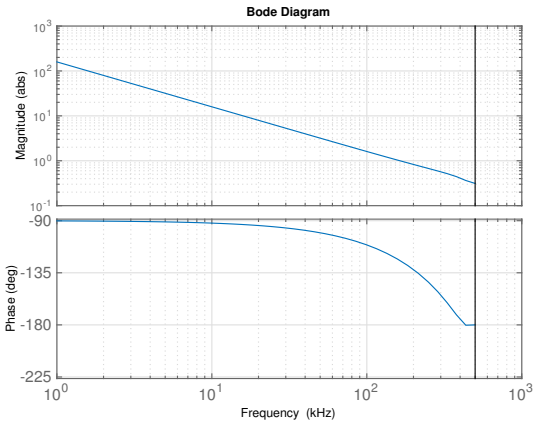

Figure 4.21 Bode diagram 2nd order.

4.4 Fiber-optic pressure sensor 1 — *Optic 1*

Figure 4.22 shows the raw data sampled at 100MHz for the fiber-optic sensor labelled *optic1*.

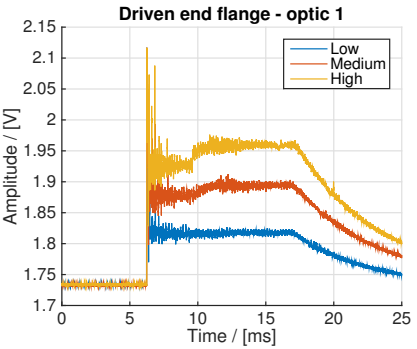

Figure 4.22 Raw data from the optic 1 sensor, sampled at 100MHz.

Data processing and impulse response analysis

Figure 4.23 illustrates the remapped data, and Figure 4.24 shows the power spectrum of the remapped data, but a resonant frequency could not be identified. Table 4.4 shows the amount of data represented by each principal component, where the first principal component has an accounting percentage of 98.5%, which is considered sufficient. Figure 4.25 and Figure 4.26 show the reconstructed signals from the first principal component and the residuals of each reconstruction respectively. Figure 4.27 to 4.29 show the residual autocovariance of each residual, and they all indicate that the residuals are not purely white for low frequencies. Figure 4.30 shows the power spectrum of the residuals and it illustrates that the residuals still contain low frequency information.

The reconstructed signals from the first principal component are averaged point by point in order to get one representative signal for impulse response analysis, see Figure 4.31. This is motivated by visual inspection of the reconstructed data which showed the signals to be exactly the same, only with an amplitude difference. The averaged signal is resampled to a reasonable lower frequency, in this case 10MHz, and the step-like start is then detected programmatically and sent to the Ho-Kalman algorithm, see Figure 4.32.

The singular values retrieved from the singular value decomposition of $H_{rs}^{(0)}$ are shown in Figure 4.33, and indicates the appropriate choice of model order. Figure 4.34 shows the result of an impulse simulation with a model of order 100. The high order is motivated by the effort to model the high-frequency behaviour of the

original data. Figures 4.36 and 4.38 illustrate the z-transform pole-zero plane and Bode diagram of the state-space system of order 100, respectively.

Figure 4.33 shows that the optic1 sensor could be modelled as simply as a system of order 3, which corresponds fairly well with the sensor model described in Section 3.6. Figure 4.35 shows the result of an impulse simulation with a model of order 3. Figures 4.37 and 4.39 illustrate the z-transform pole-zero plane and Bode diagram of the state-space system of order 3, respectively.

The 100th-order model got a goodness of fit score of 82.02%, and the third order model got a score of 63.08%. Visually, the two models seem to fit the original data well, in regards to settling value and signal curvature. The high scores indicate a good model fit, and the third-order model is considered a sufficiently good model of this sensor.

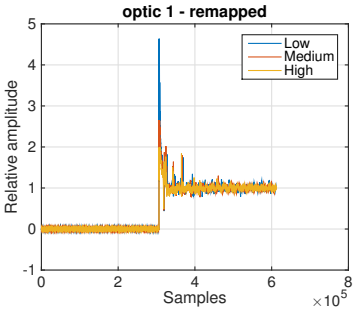

Figure 4.23 Remapped data.

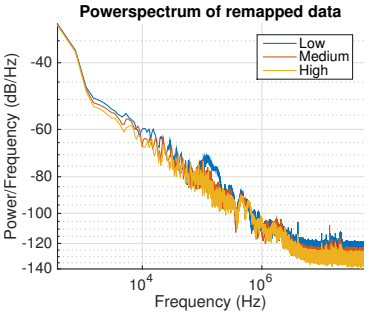

Figure 4.24 Remapped data, spectrum.

Table 4.4 Principal components, optic1 sensor.

Principal component	Accounts for
1 PC	98.5278%
2 PC	99.7175%
3 PC	100%

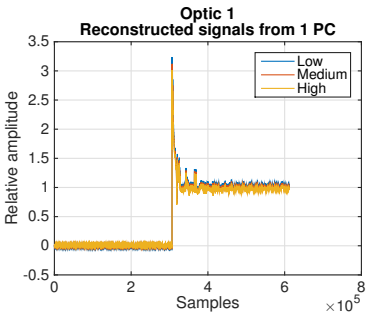

Figure 4.25 1 PC.

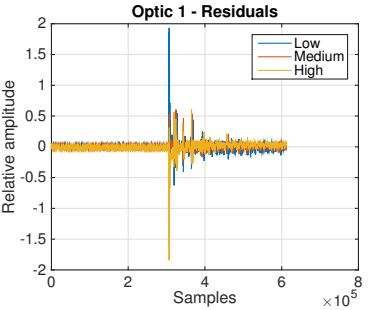

Figure 4.26 1 PC - residuals.

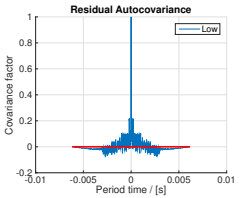

Figure 4.27 Low - resid. autocovariance.

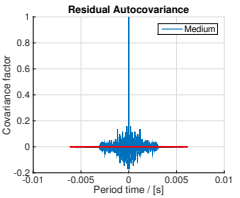

Figure 4.28 Medium - resid. autocovariance.

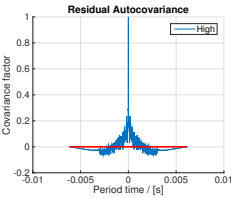

Figure 4.29 High - resid. autocovariance.

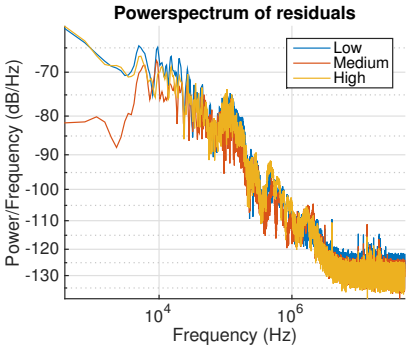

Figure 4.30 Residuals - power spectrum.

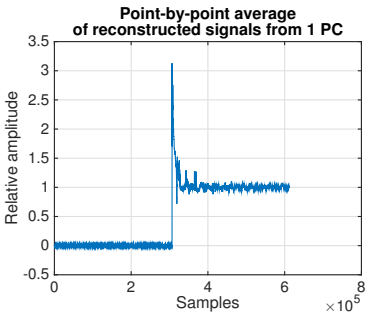

Figure 4.31 1 PC - averaged.

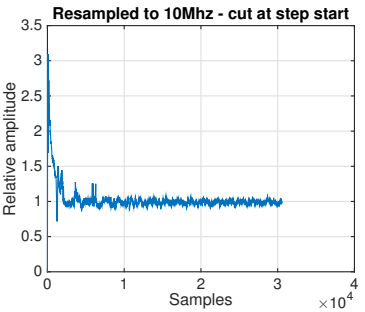

Figure 4.32 Input to Ho-Kalman.

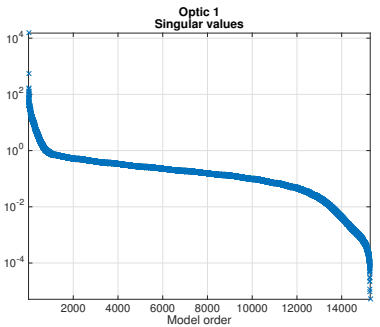

Figure 4.33 Singular values.

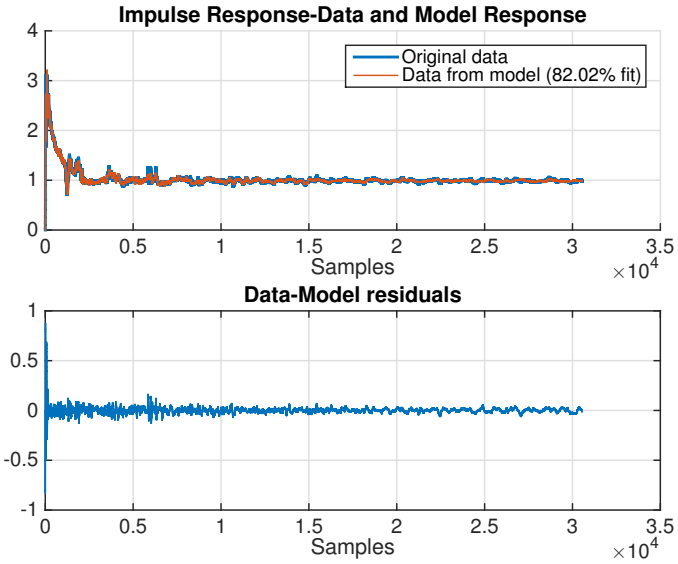

Figure 4.34 Impulse simulation 100th order.

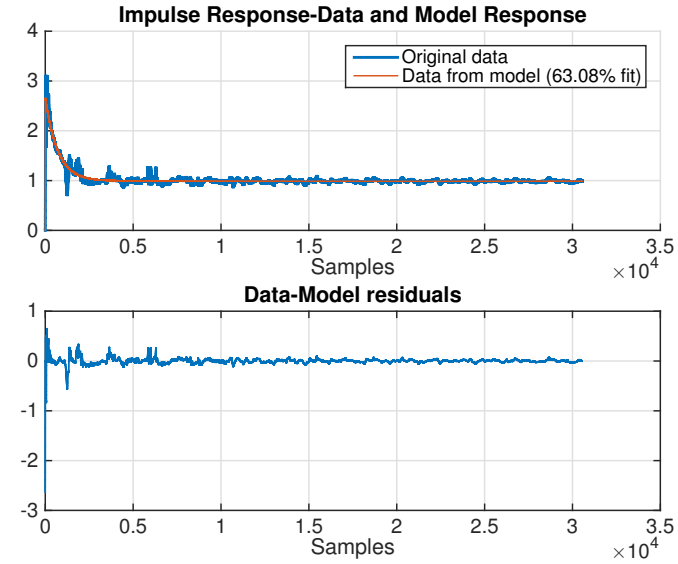

Figure 4.35 Impulse simulation 3rd order.

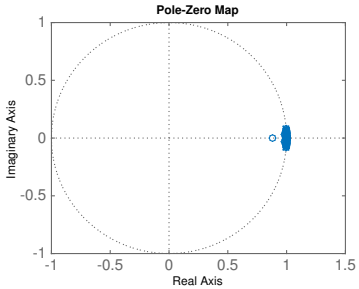

Figure 4.36 Pole-zero map 100th order.

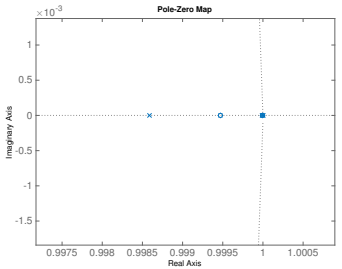

Figure 4.37 Pole-zero map 3rd order.

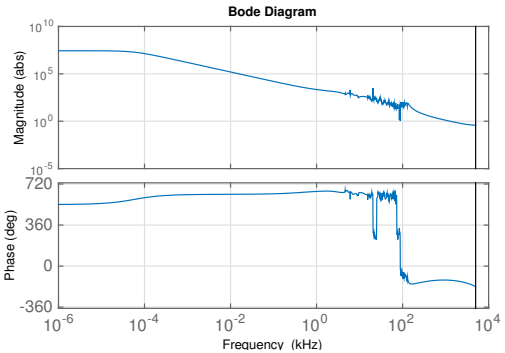

Figure 4.38 Bode diagram 100th order.

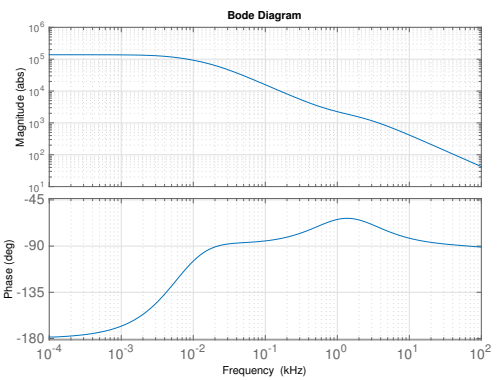

Figure 4.39 Bode diagram 3rd order.

4.5 Fiber-optic pressure sensor 2 — *Optic 2*

Figure 4.40 shows the raw data sampled at 100MHz for the fiber-optic sensor labelled *optic2*.

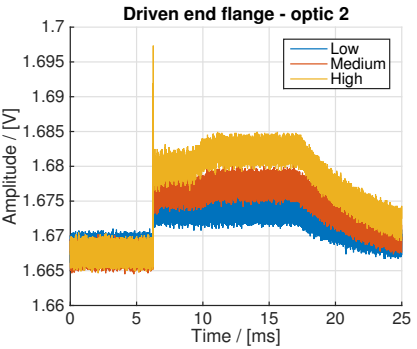

Figure 4.40 Raw data from the optic 2 sensor, sampled at 100MHz.

Data processing and impulse response analysis

Figure 4.41 illustrates the remapped data, and Figure 4.42 shows the power spectrum of the remapped data with a label indicating an identified resonant frequency at 3.11 MHz. Table 4.5 shows the amount of data represented by each principal component, where the first principal component has an accounting percentage of 98.0%, which is considered sufficient. Figures 4.43 and 4.44 show the reconstructed signals from the first principal component and the residuals of each reconstruction respectively. Figures 4.45 to 4.47 show the residual autocovariance of each residual, and they all indicate that the residuals are not purely white for all frequencies. Figure 4.48 shows the power spectrum of the residuals and it illustrates that the residuals still contain information about the resonant frequency, but also a low frequency at around 3 kHz.

The reconstructed signals from the first principal component are averaged point by point in order to get one representative signal for impulse response analysis, see Figure 4.49. This is motivated by visual inspection of the reconstructed data which showed the signals to be exactly the same, only with an amplitude difference. The averaged signal is resampled to a lower frequency with respect to the identified resonant frequency, in this case 10 MHz, and the step-like start is then detected programmatically and sent to the Ho-Kalman algorithm, see Figure 4.50.

The singular values retrieved from the singular value decomposition of $H_{rs}^{(0)}$ are shown in Figure 4.51, and indicates the appropriate choice of model order. Figure 4.52 shows the result of an impulse simulation with a model of order 50. The high

order is motivated by the effort to model the high-frequency behaviour of the original data. Figures 4.54 and 4.56 illustrate the z-transform pole-zero plane and Bode diagram of the state-space system of order 50, respectively.

Figure 4.51 shows that the optic2 sensor could be modelled as simply as a system of order 2, which corresponds quite well with the sensor model described in Section 3.6. Figure 4.53 shows the result of an impulse simulation with a model of order 2. Figures 4.55 and 4.57 illustrate the z-transform pole-zero plane and Bode diagram of the state-space system of order 2, respectively.

The 50th-order model got a goodness of fit score of 21.14%, and the second-order model got a score of 1.42%. Visually, the two models seem to fit the original data well, in regards to settling value and signal curvature. The low score could be explained by the original data having a low signal-to-noise ratio.

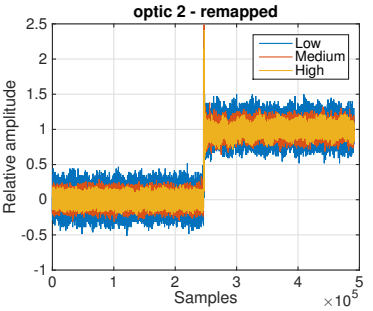

Figure 4.41 Remapped data.

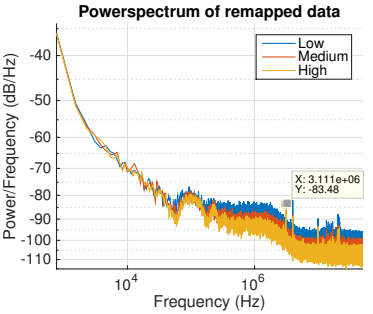

Figure 4.42 Remapped data, spectrum.

Table 4.5 Principal components, optic2 sensor.

Principal component	Accounts for
1 PC	97.9927%
2 PC	99.3397%
3 PC	100%

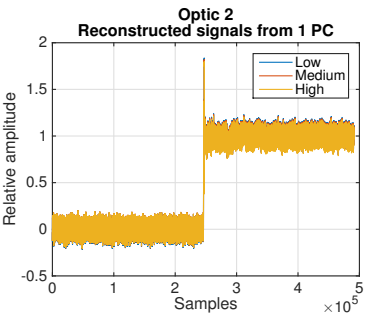

Figure 4.43 1 PC.

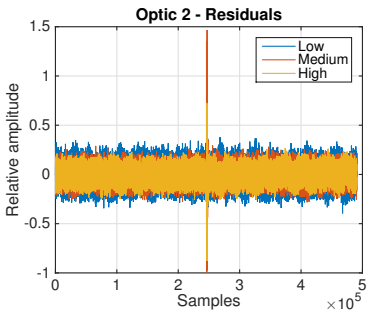

Figure 4.44 1 PC - residuals.

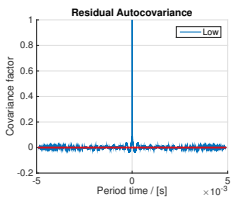

Figure 4.45 Low - resid. autocovariance.

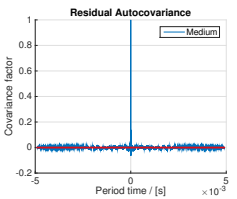

Figure 4.46 Medium - resid. autocovariance.

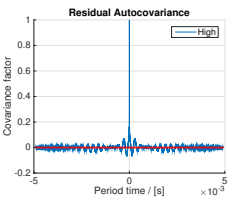

Figure 4.47 High - resid. autocovariance.

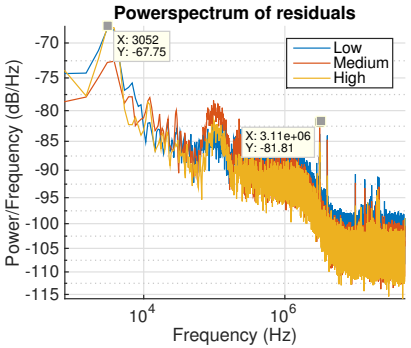

Figure 4.48 Residuals - power spectrum.

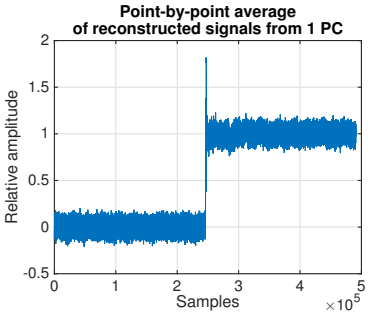

Figure 4.49 1 PC - averaged.

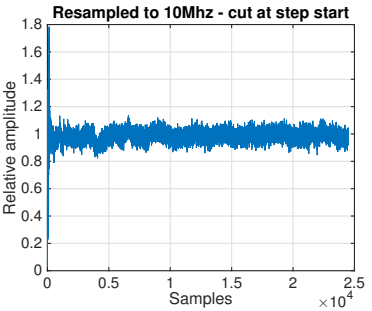

Figure 4.50 Input to Ho-Kalman.

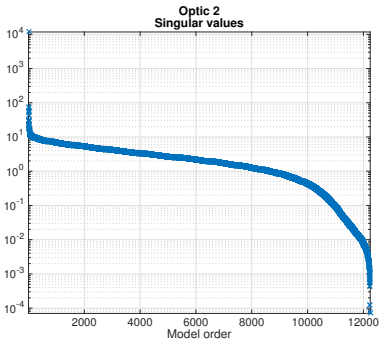

Figure 4.51 Singular values.

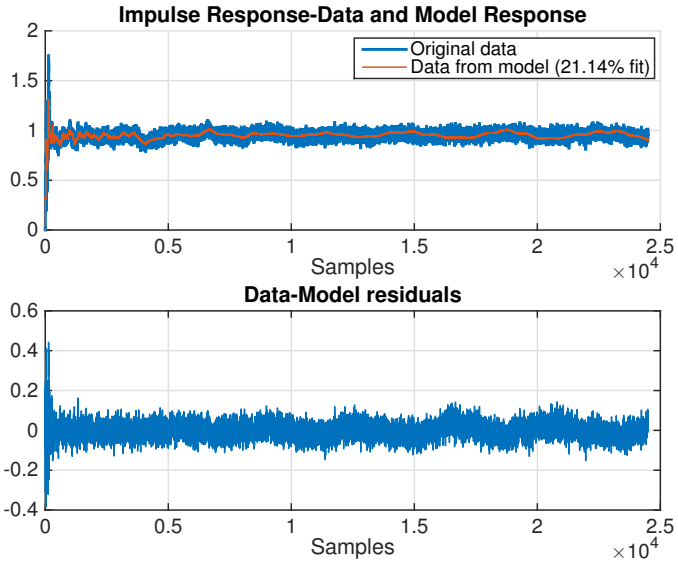

Figure 4.52 Impulse simulation 50th order.

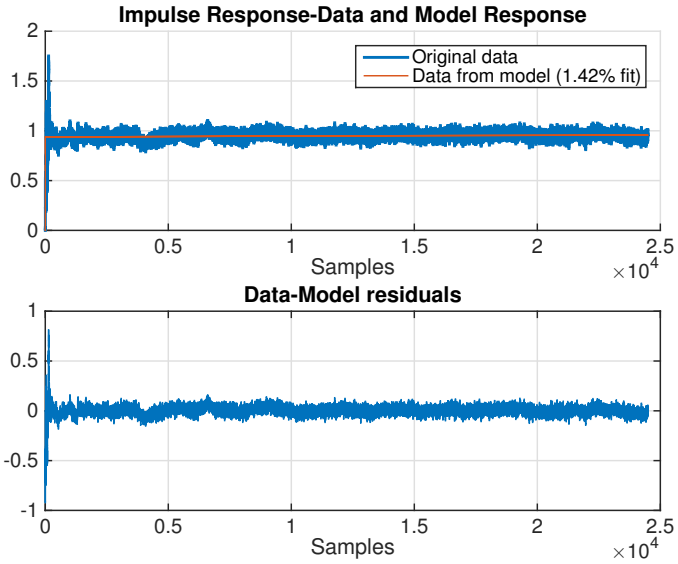

Figure 4.53 Impulse simulation 2nd order.

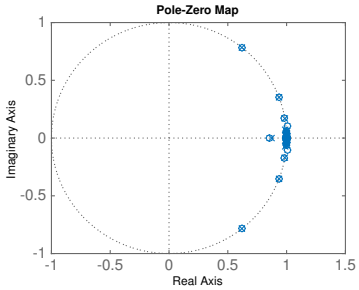

Figure 4.54 Pole-zero map 50th order.

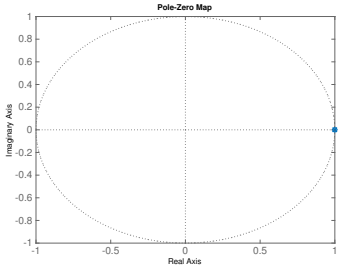

Figure 4.55 Pole-zero map 2nd order.

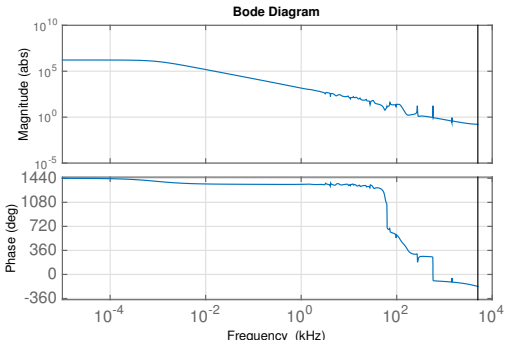

Figure 4.56 Bode diagram 50th order.

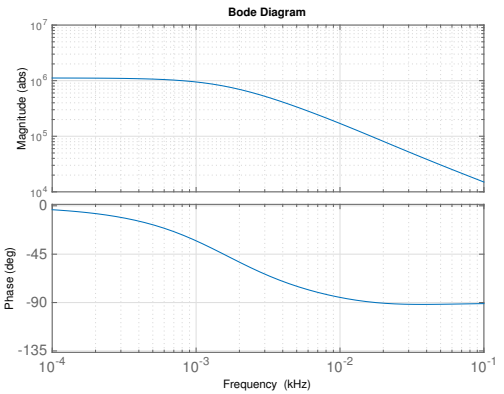

Figure 4.57 Bode diagram 2nd order.

4.6 Fiber-optic pressure sensor 3 — *Optic 3*

Figure 4.58 shows the raw data sampled at 100MHz for the fiber-optic sensor labelled *optic3*.

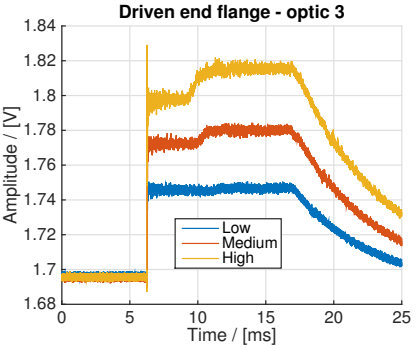

Figure 4.58 Raw data from the optic 3 sensor, sampled at 100MHz.

Data processing and impulse response analysis

Figure 4.59 illustrates the remapped data and Figure 4.60 shows the power spectrum of the remapped data with a label indicating an identified resonant frequency at 2.33 MHz. Table 4.6 shows the amount of data represented by each principal component, where the first principal component has an accounting percentage of 99.9%, which is considered sufficient. Figures 4.61 and 4.62 show the reconstructed signals from the first principal component and the residuals of each reconstruction respectively. Figures 4.63 to 4.65 show the residual autocovariance of each residual, and they all indicate that the residuals are not purely white for low frequencies. Figure 4.66 shows the power spectrum of the residuals and it illustrates that the residuals still contain information about the resonant frequency, but also a low frequency at around 6.8 kHz.

The reconstructed signals from the first principal component are averaged point by point in order to get one representative signal for impulse response analysis, see Figure 4.67. This is motivated by visual inspection of the reconstructed data which showed the signals to be exactly the same, only with an amplitude difference. The averaged signal is resampled to a lower frequency with respect to the identified resonant frequency, in this case 10 MHz, and the step-like start is then detected programmatically and sent to the Ho-Kalman algorithm, see Figure 4.68.

The singular values retrieved from the singular value decomposition of $H_{rs}^{(0)}$ are shown in Figure 4.69, and indicates the appropriate choice of model order. Figure 4.70 shows the result of an impulse simulation with a model of order 100. The high order is motivated by the effort to model the high-frequency behaviour of the

original data. Figures 4.72 and 4.74 illustrate the z-transform pole-zero plane and Bode diagram of the state-space system of order 100, respectively.

Figure 4.69 shows that the optic3 sensor could be modelled as simply as a system of order 2, which corresponds quite well with the sensor model described in Section 3.6. Figure 4.71 shows the result of an impulse simulation with a model of order 2. Figures 4.73 and 4.75 illustrate the z-transform pole-zero plane and Bode diagram of the state-space system of order 2, respectively.

The 100th-order model got a goodness of fit score of 74.96%, and the second order model got a score of 50.29%. Visually the two models seems to fit the original data well, in regards to settling value and signal curvature. The high scores indicates a good model fit, and the second-order model is considered a sufficiently good model of this sensor.

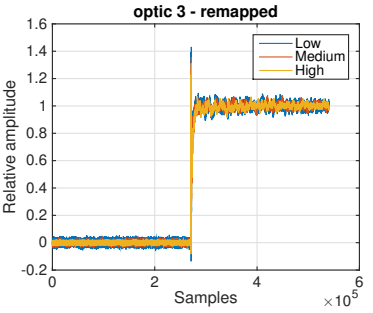

Figure 4.59 Remapped data.

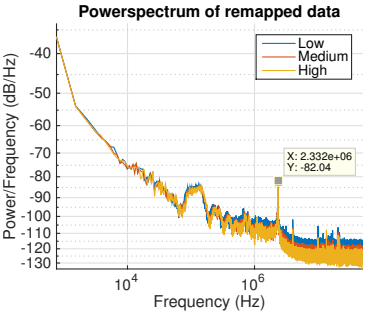

Figure 4.60 Remapped data, spectrum.

Table 4.6 Principal components, optic3 sensor.

Principal component	Accounts for
1 PC	99.8856%
2 PC	99.95%
3 PC	100%

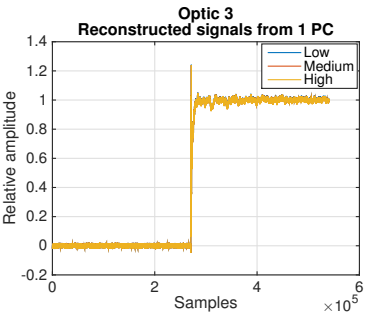

Figure 4.61 1 PC.

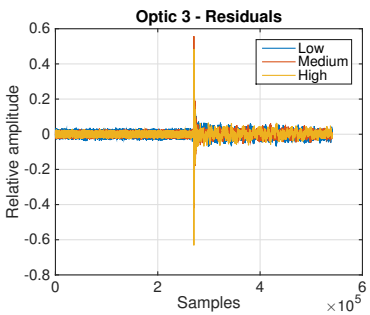

Figure 4.62 1 PC - residuals.

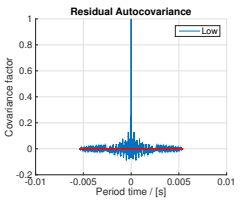

Figure 4.63 Low - resid. autocovariance.

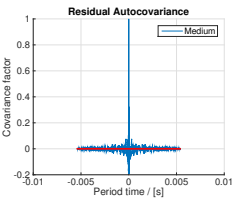

Figure 4.64 Medium - resid. autocovariance.

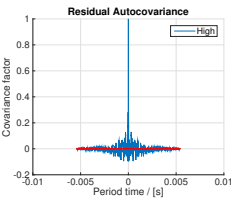

Figure 4.65 High - resid. autocovariance.

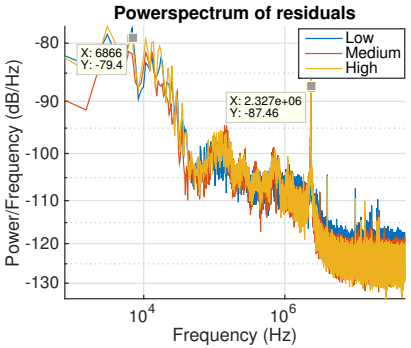

Figure 4.66 Residuals - power spectrum.

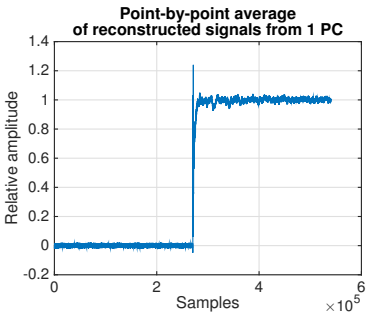

Figure 4.67 1 PC - averaged.

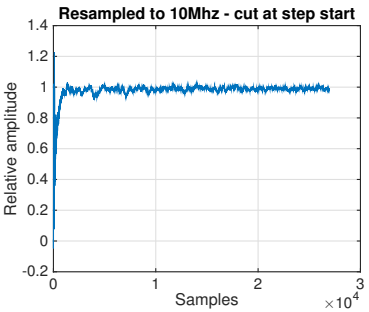

Figure 4.68 Input to Ho-Kalman.

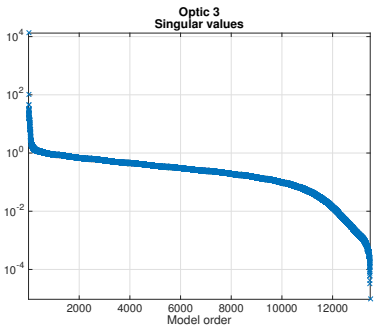

Figure 4.69 Singular values.

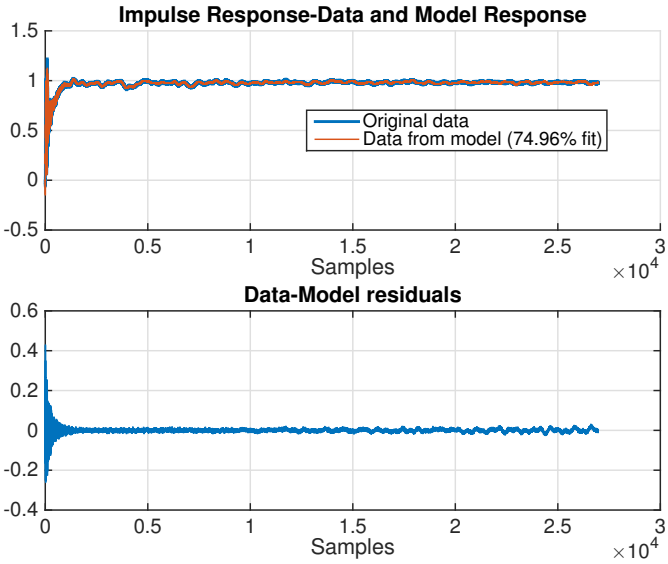

Figure 4.70 Impulse simulation 100th order.

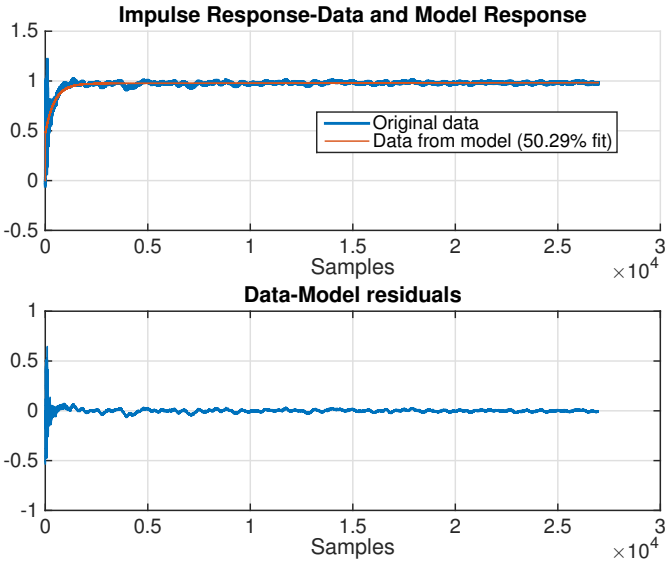

Figure 4.71 Impulse simulation 2nd order.

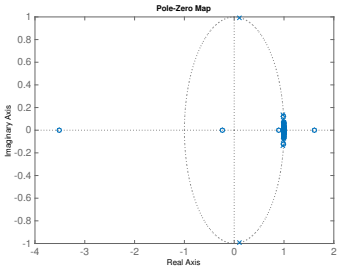

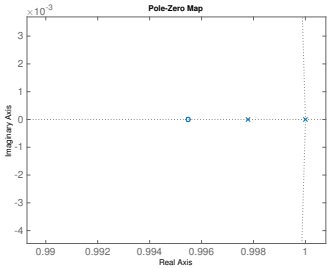

Figure 4.72 Pole-zero map 100th order. **Figure 4.73** Pole-zero map 2nd order.

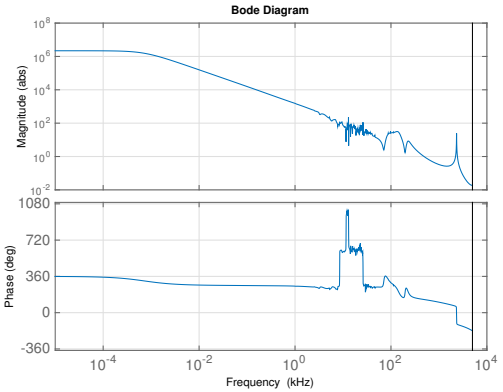

Figure 4.74 Bode diagram 100th order.

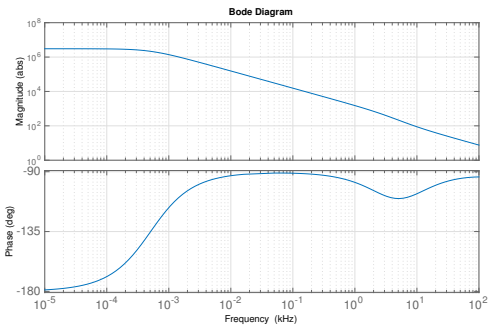

Figure 4.75 Bode diagram 2nd order.

4.7 Fiber-optic pressure sensor 4 — *Optic 4*

Figure 4.76 shows the raw data sampled at 100MHz for the fiber-optic sensor labelled *optic4*.

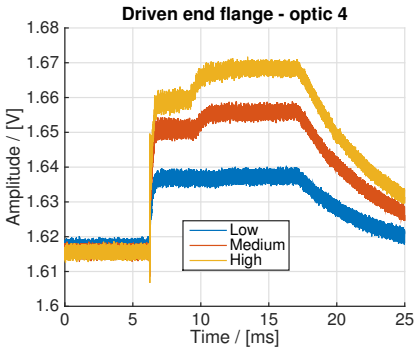

Figure 4.76 Raw data from the optic 4 sensor, sampled at 100MHz.

Data processing and impulse response analysis

Figure 4.77 illustrates the remapped data, and Figure 4.78 shows the power spectrum of the remapped data with a label indicating an identified resonant frequency at 2.78 MHz. Table 4.7 shows the amount of data represented by each principal component, where the first principal component has an accounting percentage of 99.8%, which is considered sufficient. Figures 4.79 and 4.80 show the reconstructed signals from the first principal component and the residuals of each reconstruction respectively. Figures 4.81 to 4.83 show the residual autocovariance of each residual, and they all indicate that the residuals are not purely white for all frequencies. Figure 4.84 shows the power spectrum of the residuals and it illustrates that the residuals still contain information about the resonant frequency, but also a low frequency at around 6.8 kHz.

The reconstructed signals from the first principal component are averaged point by point in order to get one representative signal for impulse response analysis, see Figure 4.85. This is motivated by visual inspection of the reconstructed data which showed the signals to be exactly the same, only with an amplitude difference. The averaged signal is resampled to a lower frequency with respect to the identified resonant frequency, in this case 10 MHz, and the step-like start is then detected programmatically and sent to the Ho-Kalman algorithm, see Figure 4.86.

The singular values retrieved from the singular value decomposition of $H_{rs}^{(0)}$ are shown in Figure 4.87, and indicates the appropriate choice of model order. Figure 4.88 shows the result of an impulse simulation with a model of order 100. The high order is motivated by the effort to model the high-frequency behaviour of the

original data. Figures 4.90 and 4.92 illustrate the z-transform pole-zero plane and Bode diagram of the state-space system of order 100, respectively.

Figure 4.87 shows that the optic4 sensor could be modelled as simply as a system of order 3, which corresponds fairly well with the sensor model described in Section 3.6. Figure 4.89 shows the result of an impulse simulation with a model of order 3. Figures 4.91 and 4.93 illustrate the z-transform pole-zero plane and Bode diagram of the state-space system of order 3, respectively.

The 100th-order model got a goodness of fit score of 91.44%, and the second-order model got a score of 83.28%. Visually, the two models also seem to fit the original data well, in regards to settling value and signal curvature. Seeing as the third order model got a high score, and a good visual fit, it is considered to be a sufficiently good model of the sensor.

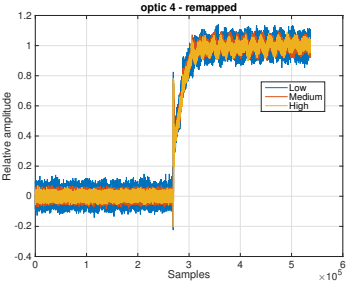

Figure 4.77 Remapped data.

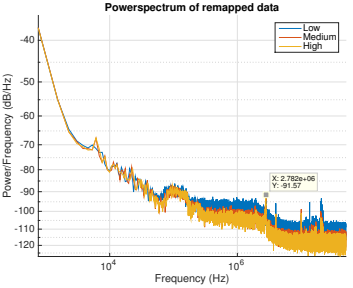

Figure 4.78 Remapped data, spectrum.

Table 4.7 Principal components, optic4 sensor.

Principal component	Accounts for
1 PC	99.7974%
2 PC	99.9461%
3 PC	100%

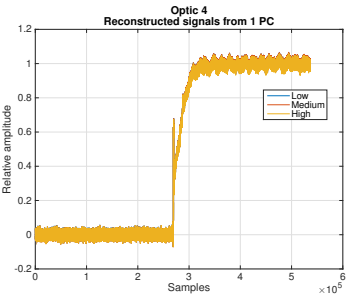

Figure 4.79 1 PC.

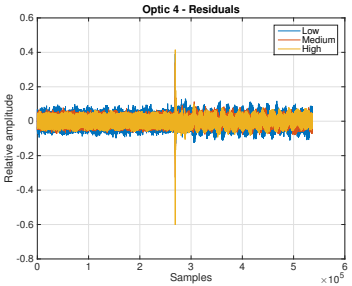

Figure 4.80 1 PC - residuals.

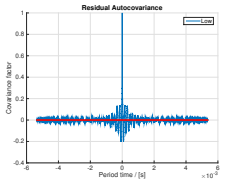

Figure 4.81 Low - resid. autocovariance.

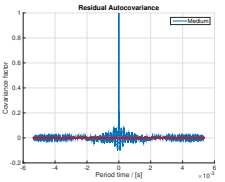

Figure 4.82 Medium - resid. autocovariance.

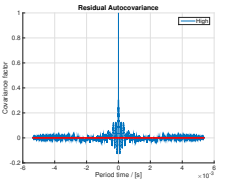

Figure 4.83 High - resid. autocovariance.

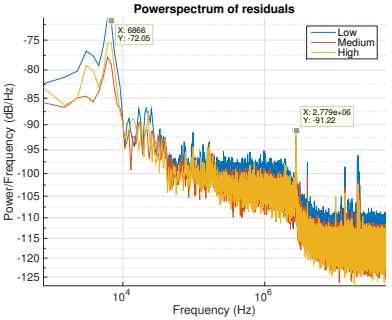

Figure 4.84 Residuals - power spectrum.

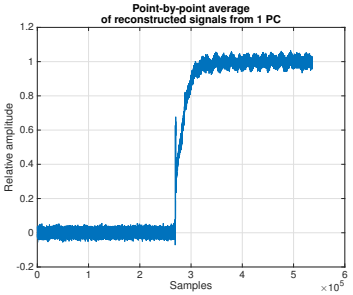

Figure 4.85 1 PC - averaged.

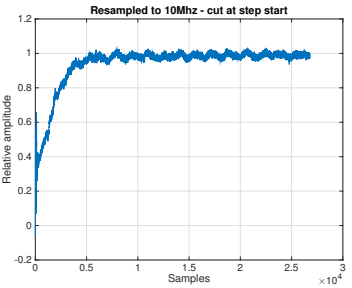

Figure 4.86 Input to Ho-Kalman.

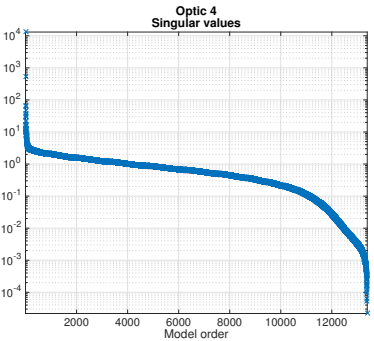

Figure 4.87 Singular values.

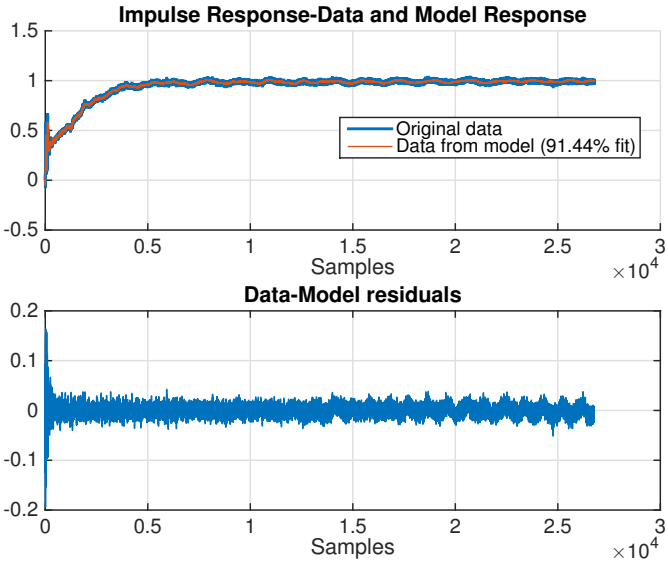

Figure 4.88 Impulse simulation 100th order.

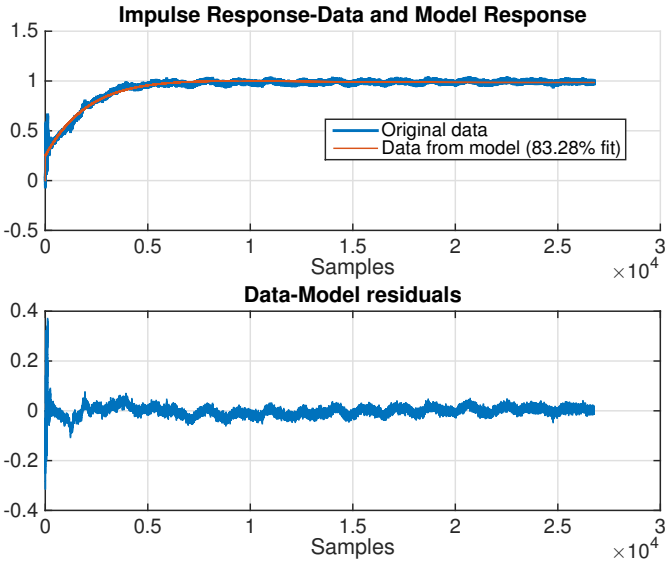

Figure 4.89 Impulse simulation 3rd order.

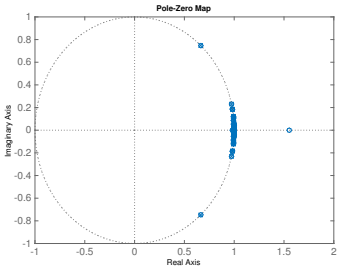

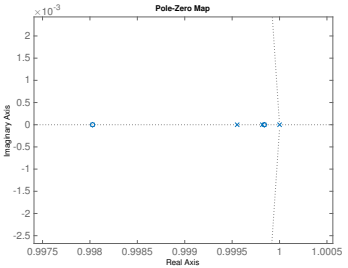

Figure 4.90 Pole-zero map 100th order. **Figure 4.91** Pole-zero map 3rd order.

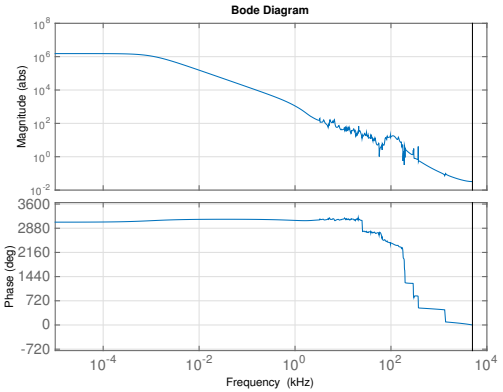

Figure 4.92 Bode diagram 100th order.

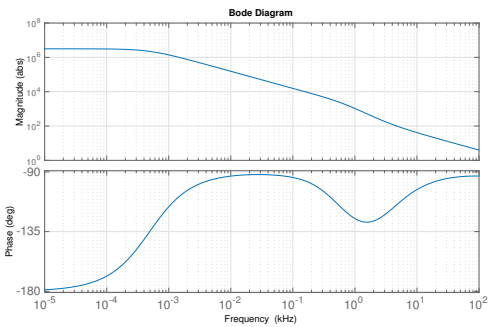

Figure 4.93 Bode diagram 3rd order.

4.8 Fiber-optic signal characteristic

Three of the four fiber-optic sensors had a unique signal behaviour, which was not detected in the signal of the piezoelectric sensor or the fiber optic sensor labelled optic1. Figure 4.94 show the signal behaviour. The source or reason for the signal's behaviour has not been determined during this thesis project, but it is included in the report since it appeared in three of the fiber-optic sensors.

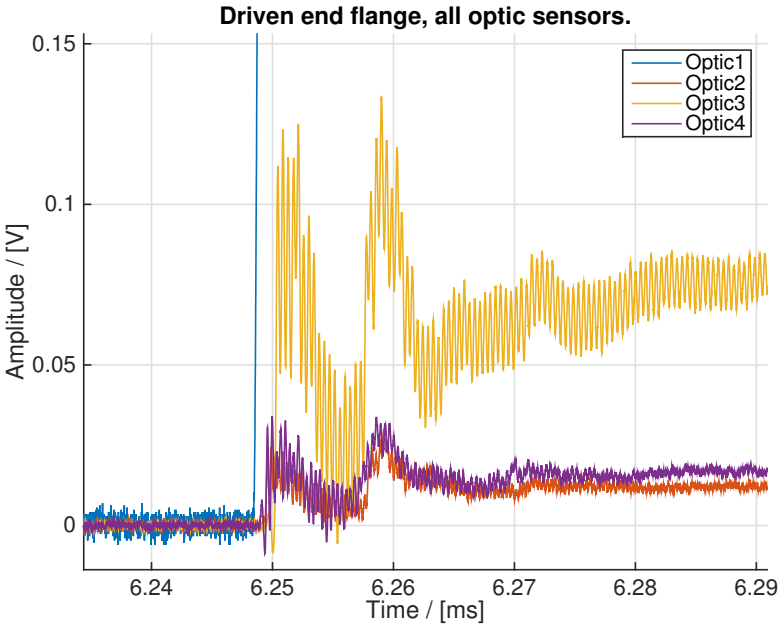

Figure 4.94 A strange signal behaviour in three of the four optic sensors.

5

Discussion

The sensors labelled optic1, optic3 and optic4 were identified with high success according to their goodness of fit scores. They even had a high goodness of fit score for the lower order model. The low goodness of fit scores for the piezoelectric sensor and the optic2 sensor is most likely caused by a low signal to noise ratio at the time of data sampling.

All the sensors showed indications of signal content in their residuals after principal component analysis. The piezoelectric sensor, optic3 sensor and optic4 sensor showed a frequency peak in the principal component residal power spectrum at 6.8 kHz, whereas the optic2 sensor showed a peak at 3 kHz. This is most likely an artefact from the principal component analysis, since the resonant frequency of the tube is much lower in frequency. An estimation of the resonant frequency is shown in Equation 5.1. In order to determine the resonance of the shock tube further experimentation would be needed. Principal component analysis is a powerful tool to use when trying to separate noise from signal, and might have been more effective if repeatable experiments could have been made.

$$f_{resonance} = \frac{v_{\text{speed of sound}}}{\lambda} = \frac{\text{Speed of sound in iron}}{2 \cdot \text{length of shock tube}} = \frac{5130}{2 \cdot 2} \approx 1282\,\text{Hz} \qquad (5.1)$$

The linear model of the sensors from Section 3.6 only models the sensors in one dimension, hence assuming the sensors only act in one dimension. When the sensors are subject to an impulse and not fastened properly in their sockets in the Driven end flange they might oscillate in two dimensions. This eventual effect has been neglected in this thesis, and the working assumption has been movement in one dimension.

The operation of the shock tube is also time consuming, but even with only a set of three measurements per sensor, three of the five sensors could be modelled with either a second or a third-order model. Even with this success the higher order models of the sensors can not be neglected, since they model high frequency behaviour that might or might not be present in a live measurement situation. With

regards to bandwidth the higher-order models of all the sensors indicate a bandwidth of 1 kHz before non-linearities appear in their Bode diagrams. Only the low-order model of the piezoelectric sensor managed to model the resonant frequency found in the power spectrum of its remapped data. Resonant frequencies usually indicate a bandwidth limit of a system.

The shock tube system can be viewed as a pipe, subject to cavity oscillations as the air inside moves back and forth. An estimation of the cavity oscillation frequencies are shown in Equation 5.2.

$$\begin{aligned} f_{resonance} &= \frac{v_{\text{speed of sound}}}{\lambda} \cdot n = [n = 1] = \frac{\text{Speed of sound in air}}{2 \cdot \text{length of shock tube}} \\ &= \frac{343.7}{2 \cdot 2} \approx 85.925\,\text{Hz} \end{aligned} \tag{5.2}$$

The estimated frequency from Equation 5.2 and multiples of the same frequency should be excluded from the sensor signal before performing system identification, in order to form a better model of each sensor. The cavity oscillation frequency would in that case have to be modelled more precisely as the speed of sound changes momentarily throughout the shock tube as the shock wave propagates, which can be seen in Table 4.2. The system identification performed on the sensors in this thesis does not account for any probable shock tube cavity oscillations.

In Section 4.8 the unique signal characteristic of three of the optic sensors is shown. The cause of this effect was not determined during this thesis project, as it could either be an effect of the shock wave only detected by the three affected optic sensors, or an artefact from the sensors or their signal conditioner.

Finally, Figure 4.19 illustrates a pole-zero plane of a second-order z-transform system for the piezoelectric sensor. The figure indicates that the system has poles and zeroes on the negative real axis of the z-plane, which typically relates to dynamic behaviour involving the Nyquist-frequency as natural frequency or resonance mode. Dynamics involving the Nyquist-frequency is more related to the sampling of the sensor than the investigated sensor dynamics. To prevent the appearance of sampling-dynamics in the low order sensor model of the piezoelectric sensor, the experiment could have been designed differently, an approach which was not tested during this project.

6

Conclusion

This thesis project has been quite successful in completing the goal of characterising the frequency behaviour of two kinds of pressure sensors, with high goodness of fit scores indicating a good model fit to impulse response data. In system identification, the impulse response test is usually only used to get an initial sense of the system to be identified in order to get information such as resonant frequencies, time delays and bandwidth before further experimentation. If higher frequency resolution is warranted, the system to be identified will have to be exposed to the desired frequencies for which to characterise its behaviour, either by exposing it to white noise containing all desired frequencies or by exposing it to discrete frequencies of interest.

Sometimes the impulse response test is sufficiently good. The results from the shock tube impulse response tests in this thesis show great promise, but the transfer functions derived for the sensors in this thesis should preferably be verified by a secondary method. One of the main problems is that the true signal would always be unknown, as the only way to measure a signal from any system is by using sensors with their own transfer functions.

Bibliography

Anderson, J. J. (2002). *Modern Compressible Flow with Historical Perspective, 3rd ed*. New York, McGraw-Hill.

Hjelmgren, J. (2002). *Dynamic Measurement of Pressure - A Literature Survey*. SP Swedish National Testing and Research Institute, SP Measurement Technology, SP REPORT 2002:34, Borås, Sweden.

Johansson, R. (2012). *System Modeling and Identification*. Department of Automatic Control, Faculty of Engineering, Lund University, Lund, Sweden.

Oakley, J. (2016). *Gas dynamics calculator - shock tube calculator*. website. http://silver.neep.wisc.edu/ shock/tools/gdcalc.html. (Accessed March 7, 2016).

Teichter, J. (2005). *Design of a shock tube*. SP Swedish National Testing and Research Institute, SP Materials Technology, SP REPORT 2005:35, Borås, Sweden.

Zelan, M. et al. (2015). *Characterization of a fiber-optic pressure sensor in a shock tube system for dynamic calibrations*. Metrologia, vol 52-1, p 48.

A

The Shock Tube

Dimensions	
Driver/Driven	97 cm
Disc thickness	3 cm
Tube inner diameter	10 cm
Total length (driver + membrane + driven)	200 cm
Sensor mount – distance between sensor and disc centre	3 cm

Sensor	function
1	Estimate speed together with sensor under test (mounted in *Sensor mount*)
2	Static pressure
Sensor mount	Sensors under test

B

Measurement setup

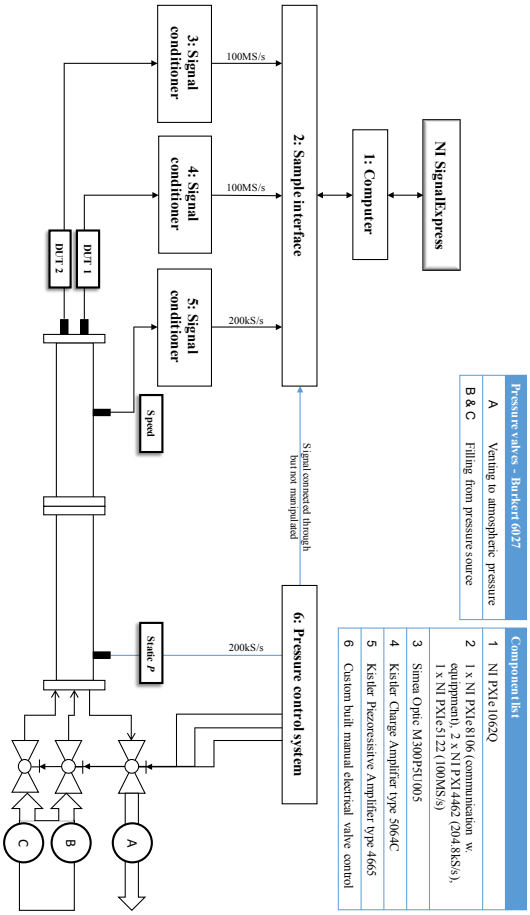

C

Photo of the setup

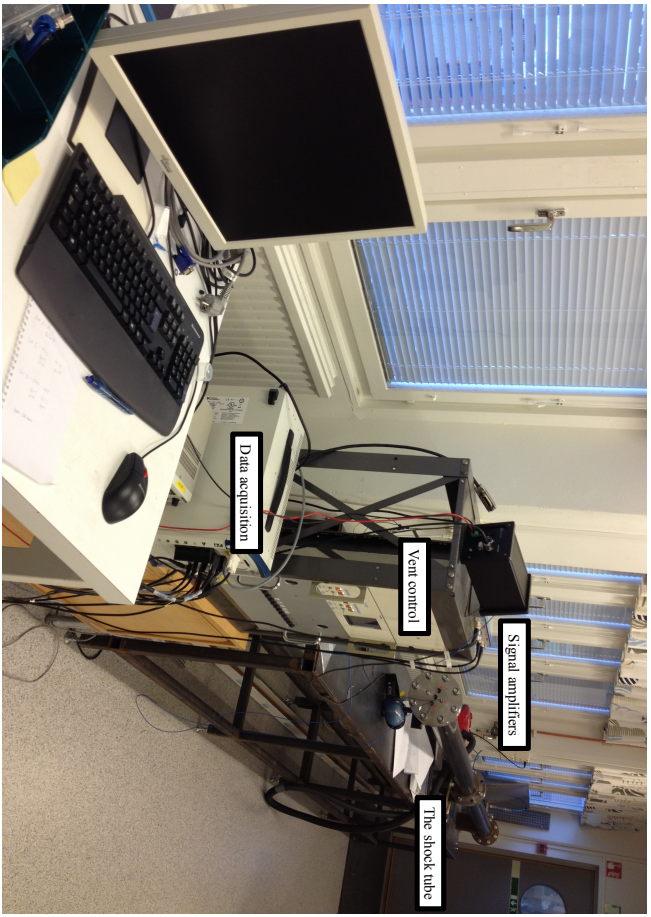

D

Matlab implementation of the Ho and Kalman algorithm

```
function [A,B,C]=impresponse(y)
%
%IMPRESPONSE
%Computes the state-space model estimate from impulse-response data y
%
%Syntax:
% [A,B,C]=impresponse(y);
%
%Input:
%  y -- impulse-response data organized as a matrix of equidistantly
%       sampled data (with base level zero).
%       impulse-response data should be organized as row vectors
%
%Output:
%  A,B,C: returned as the estimated matrices of a state-space model
%
%  x(k+1) = Ax(k) + Bu(k)      (State-space model)
%  y(k)   = Cx(k)
%
%
%Author:
%  Rolf Johansson, Lund University (Rolf.Johansson@control.lth.se)
%
%Edited:
%  Mikael Nilsson (2016-06-20), Lund University
%

figure(); stairs(y'); % plot sampled signal
N=max(size(y)); % nbr of samples
t=0:1:(N-1); % sample instances
```

```
ny=min(size(y)); % nbr of outputs from system

% H_{r,s} => r,s = floor(length(samples)/2)-1
nr = floor(N/2)-1;
ns = floor(N/2)-1;

% Create Hankel matrices
H0 = zeros(nr); H1 = zeros(nr);

for i=0:nr-1
   H0(i+1,:) = y(:,i+1:nr+i); H1(i+1,:) = y(:,i+2:nr+i+1);
end

[u,s,v]=svd(H0); % compute Singular Value Decomposition

% Display model order
figure();
plot(diag(s),'x');
title('Singular values');
xlabel('Model order');
set(gca,'Yscale','log')
axis([1 length(s) min(diag(s)) max(diag(s))])

n= input('Select a model order: '); if isempty(n), n=2; end

% Create a state-space realization from chosen model order
un=u(:,1:n);
vn=v(:,1:n);
sig=sqrt(s(1:n,1:n));
eu=[1 zeros(1,ns-1)]';
ey=[eye(ny) zeros(ny,ny*(nr-1))];
A=inv(sig)*un'*(H1)*vn*inv(sig);
B=sig*vn'*eu;
C=ey*un*sig;
D=zeros(size(ny,1));

yh=dimpulse(A,B,C,D,1,size(y,2)); % Generate model output

% Calculate goodness of fit factor
goodness_of_fit = (1 - (norm(y' - yh,2)/norm(y - mean(y),2)))*100;

% Compare original data and model response
figure;
subplot(2,1,1);
stairs(t,[y' yh]);
title('Impulse Response-Data and Model Response')
legend({'Original data'; ...
['Data from model (' sprintf('%.2f%% fit',goodness_of_fit) ')']})

subplot(2,1,2);
stairs(t,y'-yh);
title('Impulse-Response Model Error'); xlabel('Time');

end
```

Lund University
Department of Automatic Control
Box 118
SE-221 00 Lund Sweden

Document name
MASTER´S THESIS

Date of issue
September 2016

Document Number
ISRN LUTFD2/TFRT--6008--SE

Author(s)
Mikael Nilsson

Supervisor
Martin Zelan, SP Sveriges Tekniska Forskningsinstitut
Rolf Johansson, Dept. of Automatic Control, Lund University, Sweden
Anders Robertsson, Dept. of Automatic Control, Lund University, Sweden (examiner)

Sponsoring organization

Title and subtitle
Dynamic Calibration of Pressure Sensors

Abstract

English
This master thesis is a project report of a system identification experiment of pressure sensors in order to characterise their frequency behaviour. The information about the frequency behaviour is for example very useful in the automotive industry, where pressure sensors are used to measure the dynamic pressures in combustion engines. The sensors are identified by means of impulse response analysis using the Ho and Kalman algorithm based on the use of Markov parameters. The sensors presented in the thesis were identified with a certain level of success, and conclusions such as resonant frequencies and bandwidth could be drawn.
This master thesis project is performed in collaboration with SP Technical Research Institute of Sweden.

Svenska
Den här rapporten redogör för systemidentifiering av trycksensorer, och genom modellering och experiment karakteriseras sensorernas frekvensbeteende. Information om trycksensorers frekvensbeteende är särskilt användbart i bilindustrin där trycksensorer används för att mäta dynamiska tryckförlopp i förbränningsmotorer. Trycksensorerna identifieras med hjälp av impulssvarsanalys via en algoritm från Ho och Kalman som använder sig av Markov-parametrar. Sensorerna som presenteras i den här rapporten identifierades med viss framgång, och egenskaper såsom resonanser och bandbredd kunde bestämmas.
Det här examensarbetet har genomförts i samarbete med SP Sveriges Tekniska Forskningsinstitut.

Keywords

Classification system and/or index terms (if any)

Supplementary bibliographical information

ISSN and key title
0280-5316

ISBN

Language
English

Number of pages
1-66

Recipient's notes

Security classification

http://www.control.lth.se/publications/